Journal of Computational Physics 248 (2013) 1–32

Contents lists available at SciVerse ScienceDirect

Journal of Computational Physics

journal homepage: www.elsevier.com/locate/jcp

Numerical comparisons of gyrokinetic multi-water-bag models

David Coulette [a,*], Nicolas Besse [a,b]

[a] Institut Jean Lamour UMR CNRS 7198, Département Physique de la Matière et des Matériaux, Université de Lorraine, Faculté des Sciences et Technologie, Campus Victor Grignard BP 70239, 54506 Vandoeuvre-lès-Nancy Cedex, France
[b] Institut Elie Cartan UMR CNRS 7502 INRIA Calvi Team, Université de Lorraine, Faculté des Sciences et Technologie, Campus Victor Grignard BP 70239, 54506 Vandoeuvre-lès-Nancy Cedex, France

ARTICLE INFO

Article history:
Received 18 December 2012
Received in revised form 6 March 2013
Accepted 30 March 2013
Available online 19 April 2013

Keywords:
Plasma instabilities
Plasma turbulence
Gyrokinetics
Water-bag

ABSTRACT

In this paper we present two new codes devoted to the study of ion temperature gradient (ITG) driven plasma turbulence in cylindrical geometry using a drift-kinetic multi-water-bag model for ion dynamics. Both codes were developed to complement the Runge–Kutta semi-lagrangian multi-water-bag code GMWB3D-SLC described in [1]. The CYLGYR code is an eigenvalue solver performing linear stability analysis from given mean radial profiles. It features three resolution schemes and three parallel velocity response models (fluid, multi-water-bag, continuous Maxwellian). The QUALIMUWABA quasilinear code is an initial value code allowing the study of zonal flow influence on drift-waves dynamics. Cross-validation test performed between the three codes show good agreement on both temporal and spatial characteristics of unstable modes in the linear growth phase.

1. Background and motivation

The success of controlled thermonuclear fusion in magnetic confinement devices such as Tokamaks requires a thorough understanding of the transport of energy and particles in the magnetized plasma where fusion reactions occur, in order to control of the energy balance required for efficient operation of the reactor. In core magnetized fusion plasmas, classical collisional transport mechanisms are in many cases superseded by so-called "anomalous" transport mechanisms, driven by micro-turbulence stemming from a wide range of instabilities. Among these instabilities, drift-wave instabilities such as ion temperature gradient (ITG) instabilities are thought to be the most likely candidates to explain the enhanced transport observed in experiments. A large research effort has be devoted in the past decades to the study of drift-waves turbulence through theoretical, experimental and numerical simulation approaches. First principles physical models of core fusion plasmas are essentially kinetic models, where all information relevant to a particle species is contained in the one-particle distribution function $f(\mathbf{r},\mathbf{v})$ in 6D phase space. In the presence of a strong magnetic field, the large time scale decoupling between the cyclotron motion around field lines and the various drift phenomena leading to drift-wave turbulence, allows one, through the gyro-averaging operation, to derive dynamical models for the distribution of guiding-centers, pseudo-particles characterized by mass, charge and magnetic moment μ, the latter being an adiabatic invariant. A detailed development of the so-called gyrokinetic framework is exposed in [2]. The guiding-center distribution function $f_\mu(\mathbf{r}, v_\parallel)$ obeys the gyroaveraged Vlasov equation

$$\partial_t f_\mu + \mathbf{V}_{GC}\cdot\nabla f + \left(\frac{dv_\parallel}{dt}\right)\partial_{v_\parallel} f = 0, \tag{1}$$

* Corresponding author. Tel.: +33 683268906.
E-mail address: david.coulette@ijl.nancy-universite.fr (D. Coulette).

0021-9991/$ - see front matter © 2013 Elsevier Inc. All rights reserved.
http://dx.doi.org/10.1016/j.jcp.2013.03.065

where μ has been subscripted to emphasize that it acts as a parameter and not a dynamical variable. Eq. (1) can be used to describe the motion of ions, electrons or both. Depending on the phenomenon under investigation, time-scale separation of the motions of the different species may allow to avoid solving explicitly the dynamics of one species. In our case, ion guiding-center dynamics is described by (1) while the electrons are considered in the $m_e \to 0$ limit. The so-called "adiabatic" electrons are perfectly confined in the directions perpendicular to the magnetic field and free to move along field-lines. Under this hypothesis, assuming $k\lambda_D \ll 1$ and $k_\perp \rho \ll 1$, closure of the system is provided by the quasi-neutrality equation with linearized polarization drift

$$Z_i n_i + Z_i \nabla_\perp \cdot \left(\frac{n_i}{B\Omega_{CI}} \nabla_\perp \phi \right) = n_e = Z_i n_{i0} e^{\frac{q_e(\phi - \langle\phi\rangle_{FL})}{k_B T_e}}, \tag{2}$$

where $\Omega_{CI} = \frac{q_i B_0}{m_i}$ is the ion cyclotron frequency, ϕ the electrostatic potential and $\langle\cdot\rangle_{FL}$ is the averaging operator along field lines. Though the system (1), (2) provides a dramatic reduction in size and complexity compared to the original $2 \times 6D$ Vlasov–Poisson system, remains a "large" problem to solve numerically. Simulation codes such as GYSELA [3–5], ORB5 [6], GENE [7], which tackle the problem of solving Eqs. (1), (2) in realistic toroidal geometry with various methods and/or additional hypotheses, requires noticeable computational resources (see [8] for a comprehensive review of gyrokinetic simulations). Multi-water-bag modeling provides a way of reducing phase space by one supplementary dimension, by considering a family of exact weak (in the distribution sense) but particular solutions of (1). Given an integer $N > 0$, we define an N-bags multi-water-bag distribution function by

$$f(\mathbf{r}, v_\parallel, t) = \sum_{\substack{j=-N \\ j\neq 0}}^{N} A_j \mathcal{H}\big(v_j(\mathbf{r}, t) - v_\parallel\big), \tag{3}$$

where $\mathcal{H}$ is the Heaviside function, $A_j (j = 1 \dots N)$ are constant positive weights and $A_{-j} = -A_j$. Space and time variations of the distribution function thus occur only through variation of the scalar fields v_j, defining the contours of the so-called "Water-bags" (see Fig. 1(a)). The form given in (3) is not the most general one for a multi-water-bag distribution: we have in our case restricted the study to multi-water-bag distributions with two monotonic branches, the rationale for this choice being that turbulence is supposed a small perturbation of a near Maxwellian equilibrium state (i.e., a unimodal bell-shaped function). The multi-water-bag concept can be generalized to any integrable and bounded total variation distribution function with a finite number of velocity variations (Fig. 1(b)). Substituting (3) in (1), yields the following: provided the contours $v_j(\mathbf{r}, t)$ are smooth, single-valued and do not cross, f is an exact weak solution of (1) if and only if the contours satisfy the system of decoupled transport equations

$$\partial_t v_j + \vec{V}_{GC}(v_j) \cdot \vec{\nabla} v_j = \left(\frac{dv_\parallel}{dt} \right)(v_j). \tag{4}$$

The $4D$ equation in phase space $(r, v_\parallel)$ is thus reduced to a system of $2N$ fluid-like transport equations in real space. Let us emphasize the fact that the multi-water-bag (MWB) distribution is an exact solution of (1), and not a mere 0th order spline approximation. Local (in time) well posedness (existence and unicity) of classical (regular) solutions for system (1)–(4) which can be recast as a hyperbolic system of first order conservation laws in several space dimensions with non-local fluxes, has been proved in [9].

From a computational point of vue, MWB modeling leads to a decoupling in parallel velocity leading to straightforward and efficient parallelization across the contours v_j. In this paper we consider only low number of bags MWB distributions, which, in addition to decoupling, rely on low $v_\parallel$ sampling rate to further reduce computing costs. Examination of the sensitivity of the model predictions with the number of bags and their initial distribution will allow us to evaluate the limits of the model in the low range of bag numbers.

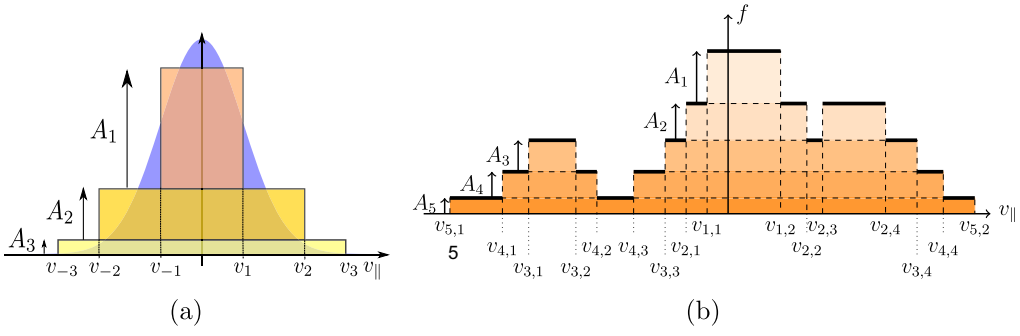

Fig. 1. Three bags MWB distribution and reference Maxwellian (a); example of a MWB distribution with five heights A_j and eight contours pairs $(v_{j,k}, v_{j,k+1})$ (b).

In [10,11], local (in the radial variable) linear studies of ITG instabilities in cylindrical geometry using the multi-water-bag model were numerically performed, while the nonlinear model (2)–(4) was solved numerically in [1] using the Runge–Kutta semi-lagrangian code GMWB3D-SLC. In this paper we present the global linear analysis code CYLGYR and the quasilinear code QUALIMUWABA that were developed to provide validation and comparison basis for GMWB3D-SLC.

2. Multi-water-bag modeling of a plasma in cylindrical geometry

In this section we define the physical system under consideration and give the explicit form of the nonlinear dynamical model obtained from (2) to (4) and its main properties. Introducing a first hypothesis on the relative magnitude of nonlinear couplings, we then derive the model we refer to as "quasilinear". A second hypothesis on the characteristic time of the evolution of the (ϑ, z)-averaged fields, allows us to derive the "adiabatic-linear" model.

2.1. Nonlinear MWB model

2.1.1. Model equations derivation

We consider here a plasma consisting in a population of ion of mass m_i and charge $q_i = Z_i e$ in the drift-kinetic limit ($\mu \to 0$), and electrons of mass m_e and charge $q_e = -e$. The plasma is confined in a cylindrical column of radius a and length L_z by a uniform and constant magnetic field $\mathbf{B} = B_0 \mathbf{e_z}$. The equilibrium state is characterized by density and temperature radial profiles $n(r), T(r)$. The evolution of the ion gyro-center distribution function $f_\mu = f(\mathbf{r}, v_\parallel, t)$ is given by the gyro-averaged Vlasov equation

$$\partial_t f + \frac{\mathbf{E}\times\mathbf{B}}{B^2}\cdot\nabla_\perp f + v_\parallel \partial_z f + \frac{q_i}{m_i} E_z \partial_{v\parallel} f = 0, \tag{5}$$

where the electric field $\mathbf{E}$ derives from the electrostatic potential ϕ. Electron dynamics is taken in the so-called adiabatic limit and closure is provided by the quasi-neutrality equation with polarization drift (2). All quantities are from now on normalized using the dimensioning factors given in Table 1. Separating ion density in its equilibrium and perturbed part $n_i = n_0(r) + \tilde{n}_i$, and considering $|\frac{q_e(\phi - \langle\phi\rangle_z)}{k_B T_e}| \ll 1$, Eq. (2) is linearized as

$$-\frac{1}{n_0}\nabla_\perp\cdot(n_0\nabla_\perp\phi) + \frac{1}{Z_i T_e}\left(\phi - \langle\phi\rangle_z\right) = \frac{\tilde{n}_i}{n_0} - 1. \tag{6}$$

Taking a multi-water-bag distribution of the form (3) with the normalization conventions of Table 1, we obtain in this geometry the transport equations for the contours $v_j(r, \vartheta, z, t)$

$$\partial_t v_j + \frac{1}{r}\left(\partial_r\phi\partial_\vartheta v_j - \partial_r v_j \partial_\vartheta\phi\right) + \partial_z\left(\phi + \frac{v_j^2}{2}\right) = 0, \tag{7}$$

and quasineutrality equation takes the form

$$-\frac{1}{n_0}\nabla_\perp\cdot n_0\nabla_\perp\phi + \frac{1}{Z_i T_e}\left(\phi - \langle\phi\rangle_z\right) = \frac{1}{n_0}\sum_{\substack{j=-N\\ j\neq 0}}^{N} A_j v_j - 1. \tag{8}$$

In all models depicted here, periodic boundary conditions are assumed in the ϑ and z direction, giving the cylinder the topology of a torus, and homogeneous Dirichlet boundary conditions for all non equilibrium quantities at $r = r_{\min} \approx 0$ and $r = a$. It should be noted that, as the problem is solved on an annulus and not on the whole disk (for which the only boundary is in $r = a$), we have to set a priori arbitrary boundary conditions in $r_{\min}$. As we consider equilibrium profiles with gradients strongly localized around mid-radius, we can expect the turbulent field, at least in its early development, to be mainly localized around mid-radius as well. For $m \neq 0$ azimuthal Fourier modes, cancellation of mode amplitude in $r_{\min}$ enforces azimuthal symmetry around the origin, and we can expect that the Dirichlet boundary condition will remain relevant in

Table 1
Normalization conventions used throughout the text.

Physical quantity	Normalization factor
T	$\overline{T} = T_e(r_0)$
t	$\overline{t} = \frac{1}{\Omega_{Ci}} = \frac{M_i}{Z_i e B}$
v, u	$\overline{v} = c_s = \sqrt{\frac{k_B T_e(r_0)}{M_i}}$
z, r	$\overline{L} = \rho_s = \overline{v}\overline{t} = \frac{c_s}{\Omega_{Ci}}$
ϕ	$\overline{\phi} = \frac{k_B \overline{T}}{Z_i e}$

time. As long as no strong mean radial gradients appear near the origin, quasineutrality for those modes is dominated by the $k_\vartheta^2 = (m/r)^2$ term of the Laplacian, which is strongly stabilizing near $r = 0$. For $m = 0$ modes, this is not the case: when the perturbed field reaches near $r = r_{\min}$ values, the homogeneous Dirichlet boundary condition leads to the apparition of spurious radial gradients. In all results presented hereafter, simulations time windows were restricted to avoid this effect. The system formed by Eq. (7) and (8) the aforementioned boundary conditions are referred to as nonlinear MWB model.

2.1.2. Conserved quantities

The nonlinear MWB model conserves integral quantities, a few of which are used to check numerical scheme accuracy. Integrating (7) over the whole cylinder $\mathcal{C}$ taking into account boundary conditions, we obtain a per-contour conservation law,

$$\frac{d}{dt}\int_{\mathcal{C}} v_j d\mathbf{r} = 0. \tag{9}$$

From (9), we can derive conservation laws for any functional of the form $I_{\mathcal{F}} = \int_{\mathcal{C}} \int_{-\infty}^{+\infty} \mathcal{F}(f) dv_\parallel d\mathbf{r}$. In the post-processing code we check relative variations for $\mathcal{F}(f) = \|f\|_1$ (mass), $\mathcal{F}(f) = \|f\|_2, \mathcal{F}(f) = f\ln f$ (entropy). Equivalence of L^1-norm and mass conservation is due to the fact that the multi-water-bag f is by construction definite positive. It should noted moreover that the water-bag model preserves by construction the maximum principle

$$\min f(t=0) < f(t) < \max f(t=0). \tag{10}$$

In addition to those integral invariants, total energy is conserved,

$$\frac{d}{dt}\left[\int_{\mathcal{C}} \sum_j A_j \frac{v_j^3}{6} d\mathbf{r} + \int_{\mathcal{C}} \left(\sum_j A_j v_j - n_0\right)\phi d\mathbf{r}\right] = 0. \tag{11}$$

In all test-cases considered further, conservation laws violations due to numerical dissipation are estimated, for a given global conserved quantity Q, by computing its relative variation with respect to its initial value $Q(t=0)$. As can been seen in Fig. 2, conservation laws are well respected in the initial linear phase, where small-scales nonlinear generation by the growing perturbation is negligible. In the subsequent turbulent phase, numerical dissipation of scales smaller than grid-size entails conservation laws violation.

2.2. Quasilinear MWB model

Taking into account periodicity of the boundary conditions in the (z, ϑ) variables, contours and potential fields are expanded in Fourier series

$$X(r,\vartheta,z) = \sum_{(m,n)\in\mathbb{Z}^2} X_m^n(r,t) e^{i(m\vartheta + nk_\parallel z)}, \tag{12}$$

where $k_\parallel = \frac{2\pi}{L_z}$ and $X_{-m}^{-n} = (X_m^n)^*$. Eq. (7) and (8) become

$$\partial_t v_{jm}^n = -ink_\parallel \phi_m^n - \sum_{m',n'} \frac{im'}{r}\left(\partial_r \phi_{m-m'}^{n-n'} v_{jm'}^{n'} - \partial_r v_{jm-m'}^{n-n'} \phi_{m'}^{n'}\right) - in'k_\parallel v_{jm-m'}^{n-n'} v_{jm'}^{n'} \tag{13}$$

and

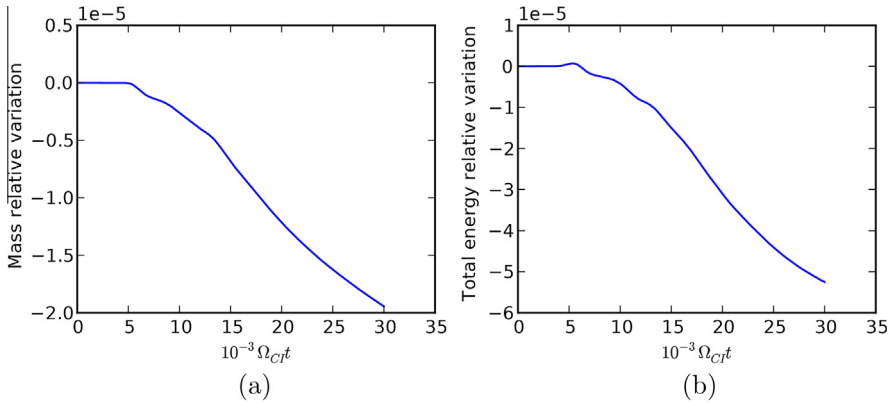

Fig. 2. Global conservation laws test for the nonlinear semi-lagrangian code GMWB3D-SLC: Evolution of relative variation with initial value of total mass (a) and energy (b) for a typical run (SMALL test-case).

$$\left[-\frac{1}{r}\partial_r r n_0 d_r + \left(\frac{m}{r}\right)^2\right]\phi_m^n + \frac{n_0}{Z_i T_e}\left(\phi_m^n - \delta\phi_n^0\phi_m^0\right) = \sum_j A_j v_{jm}^n - n_0\delta_n^0\delta_m^0, \tag{14}$$

where δ_j^i denotes the Kronecker symbol. In the quasilinear model we assume that the dominant quadratic coupling terms in (13) are those involving $(m,n)-(0,0)$ modes with $(m,n)\neq(0,0)$. This assumption is valid in the initial state, as all modes except (0,0) have vanishing amplitude, and can become invalidated later on as the turbulent field grows. Assuming all other coupling terms are negligible, we obtain the quasilinear transport equation for a Fourier mode $(m,n)\neq(0,0)$

$$\partial_t v_{jm}^n + i\left(\frac{m}{r}\partial_r\phi_0^0 + nk_\parallel v_{j0}^0\right)v_{jm}^n + i\left(nk_\parallel - \frac{m}{r}\partial_r v_{j0}^0\right)\phi_m^n = 0, \tag{15}$$

while the (0,0) mode is driven by a sum of self-coupling terms

$$\partial_t v_{j0}^0 = -i\sum_{m,n}\frac{m}{r}\left(\partial_r\phi_{-m}^{-n}v_{jm}^n - \partial_r v_j v_{j-m}^{-n}\phi_m^n\right) = -2\sum_{\substack{m>0\\ n>0}}\frac{m}{r}\partial_r\Im(\phi_m^n v_{jm}^{n*}). \tag{16}$$

The system formed of (15), (16) and (14) yields the so-called quasilinear model. As the quasi-neutrality equation takes a particularly simple form for the (0,0) mode, we can express the transport equation for the radial component of the average electric field, which equals the average poloïdal component of the drift velocity

$$\partial_t\langle v_\vartheta\rangle_{z,\vartheta} := \partial_t\partial_r\phi_0^0 = 2\sum_j A_j\sum_{m>0,n>0}\frac{m}{rn_0}\Im(\phi_m^n v_{jm}^{n*}). \tag{17}$$

It should be noted that, contrary to (15), Eq. (16) do not involve any coupling suppression. For given *identical* turbulent fields composed of $(m,n)\neq(0,0)$ modes, the evolution of the (0,0) mode would be the same in the nonlinear and quasilinear model.

2.3. Linear MWB model

Considering a situation at time t_0 where the non-(0,0) fields and their spatial variations are such that the driving term of (16) can be neglected, the (0,0) fields can then by assumed as constant in time in (15). We can then take the time Laplace transform of (15) (with $s=-i\omega=-i\omega_R+\gamma,\gamma>0$) to obtain, for an $n\neq0$ mode,

$$v_{jm}^n(\omega,r) = \frac{nk_\parallel - \frac{m}{r}d_r v_{j0}^0}{\omega - nk_\parallel v_{j0}^0 - \frac{m}{r}d_r\phi_0^0}\phi_m^n(\omega,r) + i\frac{v_{jm}^n(r,t=0)}{\omega - nk_\parallel v_{j0}^0 - \frac{m}{r}d_r\phi_0^0}, \tag{18}$$

and quasi-neutrality then becomes

$$-\frac{1}{r}\partial_r(rn_0 d_r\phi_m^n) + n_0\left(\frac{1}{Z_i T_e} + \left(\frac{m}{r}\right)^2\right)\phi_m^n = \sum_j A_j v_{jm}^n. \tag{19}$$

By substitution, system (18) and (19) can either be seen as a problem on the potential or the perturbed contours. Both formulations lead to a problem of the form $\mathcal{L}(\omega)X(\omega) = F_0(\omega)$ where $\mathcal{L}$ is a linear differential operator, non-necessarily linear in ω, X is the unknown chosen, F_0 is set by the initial condition at $t=0$. A generic solution is $X(\omega) = \sum_k X_k(\omega)\delta(\omega-\omega_k) + X_{\text{trans}}(\omega)$, where $\omega_k\in\text{Spec}(\mathcal{L})$, $X_k\in\text{Ker}(\mathcal{L}(\omega_k))$ is solution of the homogeneous system and $X_{\text{trans}}(\omega)$, the particular solution, solves the inhomogeneous problem. For arbitrary small initial conditions, provided the spectrum of $\mathcal{L}$ contains eigenvalues with $\gamma\neq0$, the solution soon becomes dominated by the unstable eigenmodes in the kernel of $\mathcal{L}$. Those unstable normal modes are the modes we seek. For each pair (m,n) of space spectral parameters, cancelling the initial condition, the system (18), (19) leads to an eigenvalue problem for the unknown radial envelopes (v_{jm}^n,ϕ_m^n). We now show how this problem can be recast following two different strategies that will lead to different solving numerical methods.

2.3.1. Formulation of the problem on the electrostatic potential

Substituting $v_{jm}^n(\omega,r)$ from (18) into (19) and cancelling initial condition, we obtain a generalized Sturm Liouville eigenvalue problem for the potential envelope $\phi_m^n(r,\omega)$, nonlinear in the spectral parameter ω,

$$\left[-\frac{1}{rn_0}d_r(rn_0 d_r) + G(m,n,\omega,r)\right]\phi_m^n(\omega,r) = 0, \tag{20}$$

with

$$G(m,n,\omega,r) = \frac{1}{Z_i T_e} + \left(\frac{m}{r}\right)^2 - \sum_j\frac{A_j}{n_0}\frac{nk_\parallel - \frac{m}{r}d_r v_{j0}^0}{\omega - nk_\parallel v_{j0}^0 - \frac{m}{r}d_r\phi_0^0}. \tag{21}$$

We can reformulate the problem in "Schrödinger" form by applying the Liouville transform $\phi_m^n = \sqrt{rn_0}\phi_m^n$, yielding the problem

$$\left[-\frac{d^2}{dr^2} + Q(r,m,n,\omega)\right]\psi_m^n = 0, \tag{22}$$

where

$$Q(r,m,n,\omega) = B(r,m) + F(r,m,n,\omega), \tag{23}$$

$$B(r,m) = \left(\frac{m}{r}\right)^2 + \frac{1}{Z_i T_e} + \frac{1}{\sqrt{rn_0}}\frac{d^2}{dr^2}\sqrt{rn_0}, = \left(\frac{m^2-\frac{1}{4}}{r^2}\right) + \frac{1}{Z_i T_e} + \frac{1}{2}\left[\frac{\kappa_n^2}{2} + \frac{\kappa_n}{r} + d_r\kappa_n\right], \tag{24}$$

$$F(r,m,n,\omega) = -\sum_j \frac{A_j}{n_0}\frac{nk_\parallel - \frac{m}{r}d_r v_{j0}^0}{\omega - nk_\parallel v_{j0}^0 - \frac{m}{r}d_r\phi_0^0} = -\sum_j \frac{\Gamma_j(r,m,n)}{\omega - \alpha_j(r,m,n)}, \tag{25}$$

with

$$\kappa_n(r) = d_r \ln(n_0), \tag{26}$$

$$\alpha_j(r,m,n) = nk_\parallel v_{j0}^0 + \frac{m}{r}d_r\phi_0^0, \tag{27}$$

$$\Gamma_j(r,m,n) = \frac{A_j}{n_0}\left(nk_\parallel - \frac{m}{r}d_r v_{j0}^0\right). \tag{28}$$

Eq. (22) with Dirichlet homogeneous boundary conditions forms the nonlinear-eigenvalue formulation of the linear MWB model.

2.3.2. Spectral linearization

Elimination of the contours envelopes led us to a smaller size problem, at the price of nonlinearity in the spectral parameter ω. We now exhibit a way of recovering the initial linearity at the price of an extension of problem dimension. Let us define for all j the unknown fields w_{jm}^n by

$$(\omega - \alpha_j)w_{jm}^n = \psi_m^n, \tag{29}$$

or equivalently

$$w_{jm}^n = \frac{A_j\sqrt{rn_0}}{\Gamma_j n_0}v_{jm}^n. \tag{30}$$

By eliminating ψ_m^n we obtain a set of $2N$ coupled equations,

$$\left[\frac{d^2(\alpha_j w_{jm}^n)}{dr^2} - (B\alpha_j + \Gamma_j)w_{jm}^n - \sum_{k\neq j}\Gamma_k w_{km}^n\right] - \omega\left[\left(\frac{d^2}{dr^2} - B\right)w_{jm}^n\right] = 0. \tag{31}$$

The problem is thus recast as a generalized eigenvalue problem on the unknown $W = (w_{jm}^n, j \in [-N,N]^*)$, linear in the spectral parameter. This formulation is referred to as the linear-eigenvalue formulation of the linear MWB model.

2.4. Linear fluid and continuous kinetic models

In order to evaluate the impact of the multi-water-bag approach on the physical predictions for the unstable modes stemming from a given equilibrium, it is necessary to compare said results against alternative models. Though comparison with external codes may provide insight on the model influence, it may prove difficult to discriminate between discrepancies arising from model and solver differences. To avoid this culprit, two additional models have been implemented. The first is an elementary 3-moments fluid model with adiabatic closure. It has been chosen for its analytic simplicity and its low instability threshold, allowing for fast testing of solver and test-cases profiles. The second one is the Maxwellian continuous kinetic model, for which the ion response can be expressed as a functional of the Fried and Conte plasma dispersion function [12]. This model is valid for a Maxwellian equilibrium distribution in $v_\parallel$. Linear analysis of both models leads to the same problem as (22), the difference appearing in the ion response function through the function $F(m,n,r,\omega)$

$$F_{\text{fluid}} = \frac{k_\nu\kappa_n\omega^2 - (nk_\parallel)^2\omega + k_\nu(nk_\parallel)^2 T_i(\kappa_T - 2\kappa_n)}{\omega\left(\omega^2 - 3(nk_\parallel)^2 T_i\right)}, \tag{32}$$

Table 2
Model naming conventions; model whose numerical results are presented are printed in boldface.

Models	Hypotheses/spectral decomposition			Driving equations	
	$\frac{\lvert X^n_m\rvert}{\lvert X^0_0\rvert} \ll 1$	$\frac{\lvert\partial t \ln\lvert X^0_0\rvert\rvert}{\lvert\partial t \ln\lvert X^n_m\rvert\rvert} \ll 1$	$X^n_m(r,t)$	(0,0)	(m,n)
Nonlinear (NL)	No	No	/	(13)	(13)
Quasilinear (QL)	Yes	No	/	(16)	(15)
Adiabatic QL	Yes	Yes	$\sum_q X_q(r)e^{-i\omega_q t}$	(16)	(18)
Forced QL	Yes	No	/	Import	(15)
Linear	Yes	Yes	$\sum_q X_q(r)e^{-i\omega_q t}$	Import	(18)
1-Mode linear	Yes	Yes	$X_{qmax}e^{-i\omega_{qmax}t}$	Import	(18)

$$F_{\text{kin}} = \frac{1}{T}(1+\xi Z) - \frac{k_\vartheta}{nk_\parallel\sqrt{2T}}\left(\left[\kappa_n - \frac{\kappa_T}{2}\right]Z + \kappa_T\xi(1+\xi Z)\right), \tag{33}$$

where $\kappa_n = d_r \log n$, $\kappa_T = d_r \log T$ are the normalized equilibrium gradients profiles, $k_\vartheta = \frac{m}{r}$, $\xi = \frac{\omega}{nk_\parallel\sqrt{T}}$, $Z = Z(\xi)$ is the Fried and Conte plasma dispersion function ([12]), Hilbert transform of the Gaussian,

$$Z(\xi) = \pi^{-\frac{1}{2}}\int_{-\infty}^{+\infty}\frac{\exp(-t^2)dt}{t-\xi}. \tag{34}$$

2.5. Summary of model naming conventions used throughout the text

Before detailing the numerical results, we present in Table 2 a synthetic table of the dynamical models studied hereafter and the assumptions on which they rely.

3. Numerical methods

We now present the various numerical methods applied to the models defined earlier. Methods for the nonlinear and quasilinear are described briefly, as the first was extensively described in [1] and the second makes use of well established classical schemes. A more detailed presentation of the methods used to solve the eigenvalue problems arising from the linear model is then given.

3.1. Nonlinear code and quasilinear code

3.1.1. Nonlinear semi-lagrangian code

The nonlinear code GMWB3D-SLC, has been described in [1]. It leverages a second order Runge–Kutta semi-lagrangian scheme with cubic splines for space interpolation to solve the advection Eq. (7) for the contours $v_j(r,\vartheta,z,t)$. Quasi-neutrality Eq. (8) is solved for the (θ,z) Fourier transformed modes radial envelopes by a second order centered finite difference scheme leading to LU factorization. No modifications were made to the core schemes described in [1]. The code was extended to accept input data (equilibrium profiles, normal modes perturbation data) generated externally. In-code diagnostics have been reduced to the bare minimum, i.e., periodic dumping of contours and electrostatic potential fields. A time-parallelized diagnostic code has been implemented for all post-processing, data analysis, extraction and visualization.

3.1.2. Quasilinear code

The quasilinear code QUALIMUWABA solves Eq. (15), (16) by a classical 4th order Runge–Kutta scheme in time. The quasi-neutrality radial differential operators are discretized by a second order centered finite difference scheme. Inversion of the resulting tridiagonal matrix is done through a simple double-sweep scheme (Thomas algorithm). The code is trivially parallelized on (m,n) space spectral numbers. The code can operate in full self consistent mode, where both (m,n) and (0,0) modes evolutions are computed, or in forced mode, where the (0,0) mode evolution is imposed by external data import. All further references to the quasilinear code concern operation in forced mode use as it allows for comparisons of the quasilinear and nonlinear dynamics of an (m,n) mode coupled with the same driving (0,0) mode.

3.2. Linear analysis code

Nonlinear eigenvalue problem such as (22) arise in many fields of dynamical systems simulation. Though a great number of approaches and schemes have been developed and used in the last decades, there is no such thing as a one-size-fits-all method: efficiency and convergence properties remain heavily dependent on problem size, structure and the nature of the nonlinearity. In our case, the MWB and fluid models lead to a so-called rational eigenvalue problem, as the pseudo-potential Q is a rational function of the spectral parameter ω. In the case of the continuous Maxwellian model, Q is an analytic

function of ω in the upper complex plane. Before describing the solvers, let us remind that the solutions we are interested in are the most unstable ones, for which the growth rate $\gamma = \Im\omega$ is greatest. Though the linear method described hereafter can provide a full spectrum containing both unstable ($\gamma > 0$), marginally stable ($\gamma = 0$) and damped ($\gamma < 0$) solutions, the focus of the work is be mostly on the unstable ones. Most notably, singularities arising from the poles of Q whenever ω is on the real axis would require a specific treatment which is out of the scope of the present work.

3.3. Linear analysis: nonlinear eigenproblem solver

Discretizing the radial differential operator on an uniform grid $r_i = r_{\min} + ih_r$ of size N_r by second order centered finite differences, taking into account Dirichlet homogeneous boundary conditions at $r = r_{\min}$ and $r = a$, Eq. (22) yields the following $(N_r - 2) \times (N_r - 2)$ discrete problem

$$E(\omega)\psi = \begin{pmatrix} a_1(\omega) & -1 & 0 & \cdots & \cdots \\ -1 & a_2(\omega) & -1 & 0 & \cdots \\ 0 & \ddots & \ddots & \ddots & \ddots \\ \vdots & \ddots & \ddots & \ddots & \ddots \end{pmatrix} \begin{pmatrix} \psi_1 \\ \psi_2 \\ \vdots \\ \vdots \end{pmatrix} = 0, \tag{35}$$

with diagonal elements $a_i = 2 + h_r^2 Q(r_i, \omega)$. The tridiagonal structure of the problem allows for an efficient two steps approach to solving (35): we first solve the dispersion equation $D(\omega) = \det(E(\omega)) = 0$ to get a given eigenvalue ω_k, then we obtain the matching eigenvector ψ_k by singular value decomposition (SVD) of $E(\omega_k)$.

3.3.1. Dispersion relation solver

The sparse structure of triadiagonal matrices allows for an efficient evaluation of their determinant (see [13,14]). Let E_i be a sequence of matrices of growing size $i \times i$, whose elements match those of E, i.e., $\forall (k,j) \in [1,i]^2$, $(E_i)_{kj} = E_{kj}$. Let $D_i = \det(E_i)$. Developing D_i columnwise yields the relation

$$D_i(\omega) = a_i(\omega) D_{i-1}(\omega) - D_{i-2}(\omega), \tag{36}$$

with starting conditions $D_{-1} = 0, D_0 = 1$. $D(\omega)$ can then be obtained by iterating (36) up to $i = N_r - 2$. The derivative $D'(\omega)$ can be obtained in the same iterative cycle by

$$D_i'(\omega) = a_i'(\omega) D_{i-1}(\omega) + a_i(\omega) D_{i-1}'(\omega) - D_{i-2}'(\omega). \tag{37}$$

As stated before, the eigenvalues with maximal imaginary part are the ones we are looking for. The solving strategy is a two-stages one:

- locate a rectangular closed contour in a subset of the upper complex plane, of highest position on the imaginary axis, containing only one root of D.
- refine root value by Newton method starting from the center of the rectangular domain enclosed by the contour found in the previous stage.

The localization step is obtained by a translate and split recursive scheme, starting from a large rectangular box sufficiently high in the complex plane. The solver first translates and divides vertically until the root count is non zero, then begins splitting both along the real and imaginary axis until the root count reaches one. Root counting is obtained by integrating $\frac{1}{2\pi} \frac{d\ln(D(\omega))}{d\omega}$ along the contour, which, by the argument principle, will equate the number of roots enclosed by the contour provided it does not enclose any poles of D. (The technique is similar to contour integration schemes described in [15,16].) The latter condition is ensured by setting a lower threshold on the position of the search box along the imaginary axis. The setting of this parameter, which acts as a filter on the minimum detectable growth rate, is of crucial importance for the efficiency of the scheme as the increased oscillations of the integrand lead to higher quadrature costs as the contour approaches the real axis. Once a contour containing only one zero and whose size reaches a fixed threshold is obtained, Newton refining is tried starting from the center of the enclosed domain. In case of no convergence the algorithm steps back to splitting. The scheme stops whenever Newton refining converges, contour dimensions are below required precision, or the locating procedure reaches the lower threshold without finding any root. Once a given eigenvalue ω_k has been found, SVD is performed on $E(\omega_k)$. The candidate eigenvector is the right singular vector corresponding to the lowest singular value, which should be of the order of the machine zero in modulus. Non-degeneracy is checked by comparison with the second lowest singular value.

3.4. Linear analysis: linear eigenproblem solver

Among the methods devoted to solving nonlinear eigenvalue problems, spectral linearization has been extensively used in the case of polynomial problems. In the case of the fluid and MWB models, the pseudo-potential Q, and consequently the diagonal elements of $E(\omega)$, are rational functions of ω. The problem can be made polynomial by mere multiplication by the

poles factors. It can then be linearized using standard companion-matrix schemes and recast a linear problem over an extended space. This approach has been tested but proved unfruitful, the error accumulation in this generic linearizing process perturbing the resulting spectrum too much. A specially tailored linearization scheme has thus been devised, allowing to define the pencil matrix coefficients directly from original data. Discretizing (31) with second order centered finite differences leads to the generalized eigenvalue problem $A - \omega B = 0$ in the extended $2N(N_r - 2)$ space of the w_{ji}. The problem is solved directly using the ZGGEV routine from LAPACK (QZ factorization). The complete spectrum and eigenspaces are thus obtained. As stated before, the stable part $\omega = 0$ of the spectrum must be considered with caution as the variable change defined in (29) can become singular whenever ω is real.

4. Multi-water-bag parameters settings

To be properly defined, a multi-water-bag distribution of the form (3) requires the setting of both the weights A_j and the contours v_j. In the context of a radial only dependence of the equilibrium quantities, this entails finding N weights A_j and $2N$ radial profiles $v_j(r)$ to represent the initial physical situation. As MWB parameters have no direct physical interpretation, a matching procedure must be devised to relate the latter to physically relevant quantities. For large number of bags, quadrature-like fitting procedures (as in [1,11]) can be used to match the MWB distribution with a given distribution in $v_\parallel$. This procedure can be fairly efficient for local (in the radial variable) analysis and large number of bags. Throughout this work we aim at using multi-water-bag distribution with small number of bags (typically 5–10) to fully take advantage of the computing cost reduction brought by the model, while trying to describe system dynamics as accurately as possible. An accurate representation of the initial equilibrium state is a mandatory prerequisite to achieve this goal. As physical equilibrium data is typically defined by radial profiles of various parallel velocity moments of the distribution function, the guiding principle for MWB parameter setting is moment equivalence: supposing given a set of reference moments, the multi-water-bag parameters must be set so as to minimize (in the least-square sense), and if possible cancel, the difference between MWB and reference moments, over the whole radial domain.

4.1. Moment equivalence

We consider an initial physical situation described through a set of parallel velocity moments $\mathcal{M}^C_k(r)$ profiles, which may be either given or computed if one knows the initial parallel velocity distribution function. In the following, we will restrict to an initial Maxwellian equilibrium with zero mean flow. In that case the set of moments can be expressed as

$$\begin{cases} \mathcal{M}^C_{2p+1} = 0, \\ \mathcal{M}^C_{2p} = nT^p J_{2p}, \end{cases} \tag{38}$$

where n and T are the density and temperature profiles, and J_{2p} is the normalized Gaussian moment ($J_0 = 1; J_{2p} = \frac{(2p)!}{2^p p!}, p > 0$). The corresponding parallel velocity moments for the multi-water-bag distribution function are given by

$$\mathcal{M}^{MWB}_k = \sum_{\substack{j=-N \\ j\neq 0}}^{j=N} A_j \frac{v_j^{k+1}}{k+1}. \tag{39}$$

Cancellation of odd order MWB moments can be realized trivially by imposing antisymmetry of the contours $v_{-j} = -v_j$. The even order MWB moments are given by

$$\mathcal{M}^{MWB}_{2p} = \sum_{j=1}^{N} \frac{2}{2p+1} A_j v_j^{2p+1}. \tag{40}$$

Exact moment equivalence condition up to order $2p_{max}$ is then, for all p such that $0 \leqslant p \leqslant p_{max}$ and $r \in [r_{min}, a]$,

$$\mathcal{M}^{MWB}_{2p} - \mathcal{M}^C_{2p} = 0. \tag{41}$$

To avoid tackling in its full generality the nonlinear optimization problem defined (41) with the additional constraint of strict contour ordering conservation on the whole domain, the following resolution scheme is adopted:

- Choose a reference radial position r_0 in the radial domain $]r_{min}, a[$.
- Choose a set of N positive reference nodes $v_j(r_0) = V_j$ at position r_0.
- Compute the weights A_j to satisfy exact moment equivalence at r_0.
- Extend the contours v_j for $r \neq r_0$ by homotopy continuation.

4.1.1. Local moment equivalence at r_0

For a given number of bags N, any ordered set of positive N real numbers can a priori be chosen as reference nodes $v_j(r_0) = V_j$. Those being known, problem (41) with $p_{max} = N - 1$ can be rewritten as

$$\sum_j A_j V_j (V_j^2)^p = \left(p + \frac{1}{2}\right) \mathcal{M}^C_{2p}(r_0), \quad 0 \leqslant p \leqslant N-1. \tag{42}$$

To simplify notations, we define the modified moments $\mathcal{M}^M_{2p}$ as

$$\mathcal{M}^M_{2p} = \left(p + \frac{1}{2}\right) \mathcal{M}^C_{2p}. \tag{43}$$

The $X_j = A_j V_j$ are thus solutions of a Vandermonde system of nodes (V_j^2). The Vandermonde structure has two main consequences in our case: on the one hand, deterioration of the conditioning of the solutions when N increase limits the range of accessible N values, typically around 10. On the other hand, the strongly oscillating nature of the solutions as functions of the nodes makes it difficult to ensure a priori positivity of the weights A_j. The first is not so much of a problem as we restrict ourselves to small N MWB distributions, but the second imposes severe restrictions on the initial node setting. It should be noted that individual weight positivity is not necessary for the MWB distribution to be positive, which would only require positivity of the partial sums $f_k = \sum_{j \geqslant k} A_j, k \in [1, N]$. By imposing individual weight positivity we ensure at the same time positivity and strict monotonicity of the MWB distribution function in $| \ v_\parallel \ |$, the latter taken as a safeguard against triggering of spurious instabilities. Though explicit solutions of the Vandermonde system can be expressed using Langrange interpolation polynomial coefficients (see Appendix A) and positivity conditions can be stated (see Appendix B), they are not explicit enough to define a constructive procedure to restrict the space of initial nodes. In the Maxwellian equivalence case, we can however establish necessary conditions for positivity on the extreme nodes V_1, V_N

$$V_1 < \sqrt{3}\sqrt{T(r_0)}, \tag{44}$$

$$V_N > \sqrt{2N-1}\sqrt{T(r_0)}, \tag{45}$$

which provide a minimal extension for the initial node distribution. Weights positivity is not however, the only criterion guiding initial nodes setting: for small number of bags, the $v_\parallel$ global extent and node distribution notably influence the dynamics of the system through the wave-particle resonance terms $\omega - nk_\parallel v_j$. With fewer nodes, sampling artifacts are more likely to occur. In addition to weights positivity, we must impose constraints on node support by bounding $V_1 > V_{min}$ and $V_N < V_{max}$, and distribution by restricting the nodes distances distribution dispersion. The latter condition can be enforced strongly by imposing equipartition of nodes, or more weakly by bounding the ratios V_j / V_{j-1}. One could wonder why we do not try to obtain a constraint system yielding a unique solution, i.e., force the values of both nodes and weights. This is actually possible for some values of N. By requiring exact local moment equivalence for the first $2N$ moments, we obtain a $2N$ equation system which can be recast as a generalized Hankel eigenvalue problem, as is done in [17]. This approach allows for strong local moment equivalence, but unfortunately showed poor non-local radial extensibility properties.

4.1.2. Radial extension of exact equivalence

Once a set of reference nodes $V_j = v_j(r_0)$ has been chosen and the weights A_j computed, we proceed to the computation of the radial profiles $v_j(r), r \neq r_0$. To that end, for all value of $r \neq 0$, we must solve for the unknowns $V_j = v_j(r)$ the system $S(r)$ of N polynomial equations

$$\sum_j A_j V_j^{2p+1} - \mathcal{M}^M_{2p}(r) = 0, \tag{46}$$

where p ranges from 0 to $N-1$. For each r, the multivariate polynomial system $S(r)$ can have a very large number of solutions, and the cost of a full solution would be prohibitive. Considering however that we know a particular solution of $S(r_0)$, we want to build continuous radial profiles for the v_j, and the mapping $r \to S(r)$ is continuous, we can solve it by homotopy continuation: assuming a solution $V(r)$ of $S(r)$ is known, the solution of $S(r + dr)$ is obtained by Newton method starting from $V(r)$.

- Start from known solution vector $V_1 = V(r)$.
- Until (convergence or crossing) do:
  - Compute residual vector $\Delta(V_n) = [\mathcal{M}^{MWB}(V_n) - \mathcal{M}^M(r + dr)]$.
  - Update $V_{n+1} = V_n - (J_\Delta^{-1})(V_n)$, where J_Δ is the system Jacobian matrix.

This procedure is iterated upwind and downwind from the initial known solution $V(r_0)$. The crossing condition is defined by imposing a lower bound on $\min\{V_{j+1} - V_j\}$. As the Jacobian matrix has a Vandermonde like structure, it becomes singular whenever any two nodes get too close to each other. The problem of solving the system near and after a crossing does not need to be addressed as we want to build non- crossing distributions. This non-crossing condition adds a posteriori restrictions to the set of initial nodes $v_j(r_0)$ that can be chosen as a starting point. As shown in C, the polynomial structure of the multi-water-bag moments implies limits on the extensibility of the distribution: starting from a given set of weights A_j and nodes $v_j(r_0)$, it is not possible to reach any target moment vector $\mathcal{M}^M$ with non-crossing continuous contours. The choice of

initial nodes is consequently crucial for the non-local extensibility of the distribution. This is a major restriction compared to the local case, where the only constraint is on weights positivity and adequate sampling. In the case of equivalence with a Maxwellian distribution, extensibility bounds can be more precisely defined, as Maxwellian moment space dimensionality is restricted by the dependency of the centered Maxwellian distribution on the sole density and temperature. Defining the rescaled contours $u_j(r) = v_j(r)/\sqrt{T}$, the Maxwellian prefactor $\alpha(r) = \frac{n}{\sqrt{T}}$,and $K_{2p} = (p + \frac{1}{2})J_{2p}$ the exact moment equivalence equation at order p becomes

$$\sum_j A_j u_j^{2p+1}(\alpha) = \alpha K_{2p}. \tag{47}$$

The problem of radial extensibility is thus restricted to the problem of α extensibility. This property allows one to try and find initial nodes $v_j(r_0)$, used as starting points for the weights computation and homotopy continuation procedure described earlier, that optimize α extensibility, regardless of the exact nature of density and temperature profiles. This type of initial nodes $v_j(r_0)$ is required for gradient profiles scan studies, where we want to be able to vary equilibrium profiles, while keeping initial node distribution constant to preserve continuity in the mapping $(n, T) \to v_j$.

4.2. Sample equilibrium test-cases

We now present the various test-cases used as a basis throughout numerical experiments. They are first grouped in three families based on radial domain size, unsurprisingly named SMALL, MEDIUM and BIG. In all cases, the reference density and temperature profiles are staircase-shaped ones (Fig. 3) defined by

$$X(r) = \exp\left(\kappa_X \Delta_{r_X} \tanh\left(\frac{r - r_X}{\Delta_{r_X}}\right)\right), \tag{48}$$

where the parameters $\kappa_X, \Delta_{r_X}, r_X$ allow to control respectively the normalized gradient peak height, width and position. Values of the parameters for the reference cases are given in Table 3. For each family, parametric studies are done by varying one or more parameters, domain size excepted, from this base parameter sets. From Figs. 3 and 4, using the exact moment equivalence method, we observe agreement of the reference and MWB moments and gradients up to machine precision. This property ensures no distortion is introduced by the MWB distribution building procedure in the equilibrium physical characteristics. It should be noted that the chosen sets of equilibrium parameters are not meant to depict realistic fusion devices plasmas: the strongly localized gradient zones and small domain sizes were chosen to obtain well localized turbulent fields and the necessary radial resolution while minimizing the required computing and storage costs.

5. Linear and quasilinear analysis codes validation

Numerical methods and models for the linear problem described in Section 3 have been implemented in the CYLGYR linear analysis code. Independence of the linear problem for different (m, n) parameters pairs allows for a simple parallelization scheme, where the various (m, n) pairs are statically dispatched among available processes. Several validation approaches were adopted:

- For a given resolution scheme, we check convergence of results with radial resolution, and bags number.
- We check consistency of results between the nonlinear and linear eigenvalue solvers.
- We perform cross validation of the linear spectral code with the quasilinear initial value code.

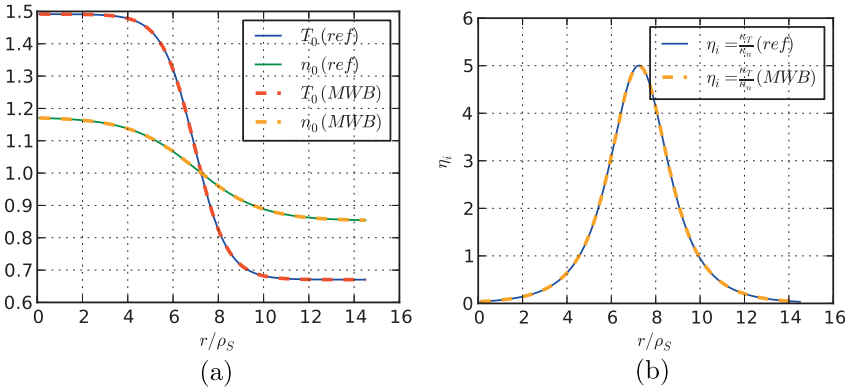

Fig. 3. Density and temperature radial profiles (a) and η_i radial profile (b) for the MEDIUM case. Analytical reference profiles and multi-water-bag ones fit to machine precision.

Table 3
Reference cases parameters set.

	Small	Medium	Big
$r_{\min}/\rho_s$	1	0.1	0.1
$r_{\max}/\rho_s$	9	14.5	20
N_r	128	128	128
Index r_0	64	64	64
κ_n	10^{-2}	$5.51 \cdot 10^{-2}$	10^{-2}
Δ_{r_n}	2	2.9	4
κ_T	10^{-1}	$2.7586 \cdot 10^{-1}$	10^{-1}
Δ_{r_T}	0.3	1.45	2
$k_\parallel$	10^{-3}	$4.17 \cdot 10^{-3}$	10^{-3}
N_{bag}	6	6	6

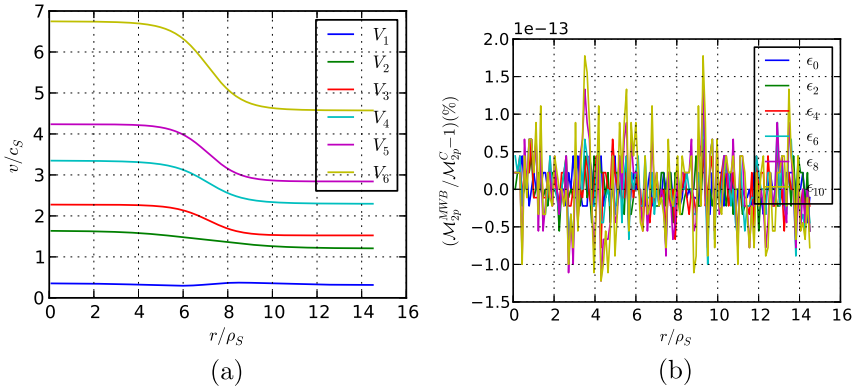

Fig. 4. Radial profiles of positive bags contours (a) and moments relative error (b) for the MEDIUM test-case.

- We compare results obtained for various models (MWB, Continous Maxwellian) from a common equilibrium.
- We compare the (radially) global method with a local method using an ansatz for the solution vector ϕ.

5.1. Convergence tests

5.1.1. Radial sampling width convergence

Growth rates (Fig. 5(right)) typically converge (with relative variations below 1%) when $h_r \approx 0.1\rho_s$. Frequencies convergence (Fig. 5(right)) is usually faster, with a $h_r \approx 0.4\rho_s$ for the same maximum relative variation. For realistic sampling width range, both growth rates and frequencies exhibit strictly monotonic convergence, increasing in absolute value. Undersampling thus leads to a slight underestimation of growth rates and frequencies.

5.1.2. Pseudo-convergence with respect to number of bags

As stated in Section 4, even requiring exact moment equivalence for N moments, for a given number of bags N, density and temperature profiles are not sufficient to determine a unique MWB distribution function. As the current work focuses on small number of bags distributions, it can be expected that the position and distribution of initial nodes in $v_\parallel$ space have a non negligible impact on the results. To speak of convergence with number of bags, one should ideally perform for each value of N an extensive scanning of admissible distribution functions, and show that the dispersion of results for a given N is lower than the dispersion of the results between N and $N+1$ bags distributions. As this approach would prove too costly, we restrict the study of the influence of bag number to a purely empirical approach: we observe the evolution of results, examine if tendencies emerge, without aiming at conclusive assertions. Moreover, restrictions on initial nodes choice arising from the weights positivity and non-crossing requirements prevent us from obtaining an clearly increasing sampling density with N. As expected, no global convergence pattern can be observed. For small values of the spectral number n though, growth rates and frequencies tend to converge monotonically (Fig. 6(a)), while this tendency is lost for large n values (Fig. 6(b)). This higher sampling sensitivity of results with growing parallel frequency is to be confirmed by the comparison with alternative models.

5.2. Consistency of nonlinear and linear solvers

The nonlinear and linear eigenvalue problems (22) and (31), though not strictly equivalent, should provide consistent results for the most unstable modes we seek. Eigenvalues and eigenmodes obtained from the two methods show good agree-

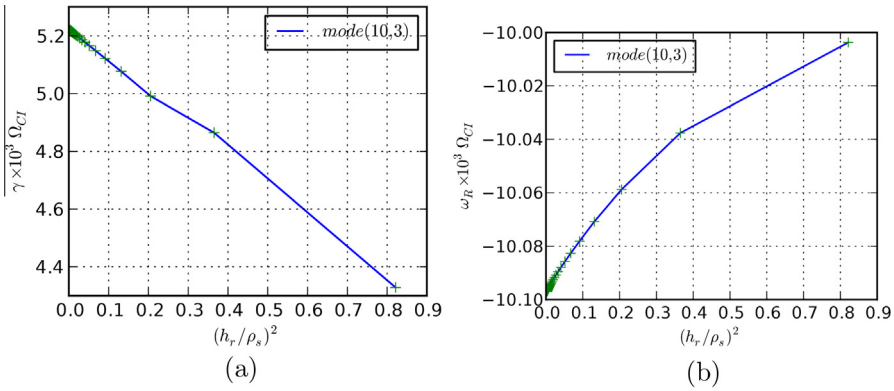

Fig. 5. MEDIUM test case – radial sampling dependency of the most unstable mode $(10, 3)$.

ment for most of the (m, n) plane, with relative errors on growth rates and frequencies ranging from 10^{-9} to 10^{-5}. (see Tables 4,5 and Fig. 7). Discrepancies can appear for $nk_{\|}$ fringe modes, at the border of the unstable (m, n)-zone. Here we have compared for each (m, n) pair the most unstable mode obtained by both solvers. For most (m, n) pairs, one eigenvalue clearly dominates all others, but for some low m modes, a chain of secondary eigenvalues of nearly equal frequency and decreasing growth rates can be found (see Fig. 8(a)). Those modes are not artifacts of the linearization process, as can be checked in the $(13, 1)$ mode case (8(b)) where the argument variations of the nonlinear dispersion relation and the eingenvalues from the linear solver show good agreement for all secondary eigenvalues.

5.3. Cross validation with quasilinear code

Once eigenmodes for a given equilibrium have been obtained, we can build perturbed states by adding to equilibrium quantities any linear combination of such modes. Setting the quasilinear code with this initial perturbed state and maintaining artificially the (0,0) quantities to their equilibrium values, we obtain a non-saturating unbounded linear-growth phase, allowing for accurate check of growth rate, frequencies, and radial envelopes. Conversely, this allows one to check the stability of the quasilinear forced mode scheme with the time sample widths we can expect to use when performing the comparisons between the quasilinear and the nonlinear code presented in the next section. Those sample time widths are fixed by the nonlinear code diagnostic frequency, and are of the order of $10\Omega_{CI}^{-1}$. Growth rates for the quasilinear code are obtained by logarithmic regression on global $(\|\phi\|_2, \|\phi\|_\infty)$ and local $(\mid \phi \mid (r_0))$ quantities. Frequencies are obtained by time fast Fourier transform from local $\cos(\arg(\phi(r_0, t)))$. We observe good agreement between linear and quasilinear values with relatives errors of the order of 10^{-3} to 10^{-2} (see Table 6). Envelope geometry is slightly perturbed during the initial transitory regime, then locks back to the linear one. Quantitative comparison is done by following $\| \frac{\phi_{ql}}{\|\phi_{ql}\|_\infty} - \frac{\phi_{\text{lin}}}{\|\phi_{\text{lin}}\|_\infty} \|_\infty$ over time and, for envelopes that are well localized, checking the times evolution of the on-grid (discrete) maximum and the first geometric moments to get position and peak width values. The agreement is good: the relative error between linear and quasilinear position and width parameters is of the order of 10^{-3} , with absolute errors below radial grid step size. After a slight curvature distortion in the initial transitory regime, the radial envelope stabilize, with a maximum relative error of a few percent. Radial variation of envelope phase $Arg(\phi(r))$ is also well preserved.

5.4. Comparison between various models

Having checked the validity of the linear solvers for the MWB model, we can now examine the sensitivity of the linear eigenstructure to the form obtained in the various models for the density linear response $\tilde{n}_i(\omega)$. The fluid model, as expected yields larger growth rates and larger unstable span in (m, n) space than the others, while the real frequencies ω_r and eigenmode geometry stay closer to those of the others models. We focus here on comparing the various MWB models with the Maxwellian kinetic continuous model, taken as a reference solution. Using the three equilibrium test-cases, the MWB distributions were generated for a number of bags ranging from 4 to 10, using for each bag number two methods of initial nodes generation: the first optimizing radial extensivity, the second using a uniform node repartition in parallel velocity. The last is referred to as "iso-V" MWB distributions.

5.4.1. Growth rates and frequencies

Two general observations emerge from the results of the model scan. On the first hand, relative errors for the real frequencies between models tend to be lower than those on growth rates. On the second hand, relative errors on both frequencies and growth rates show little variation with m and grow with n. All models tend to agree for low n values, discrepancies appearing as n grows. This has a strong impact on the high n cutoff wavenumber of the instability, enhanced by the discrete

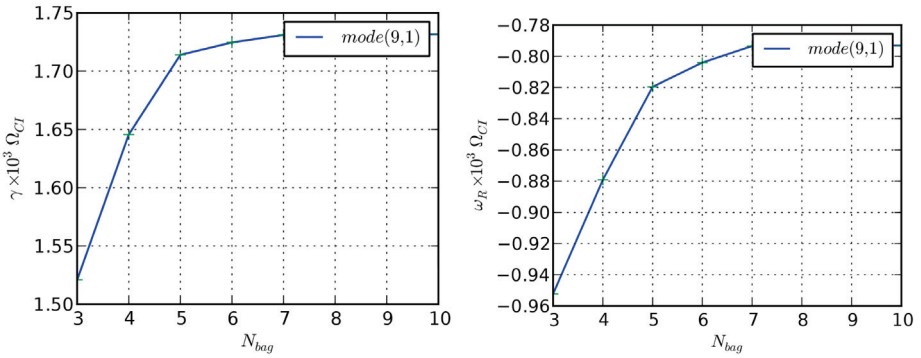

(a) BIG case ; Pseudo-Convergence for low n modes

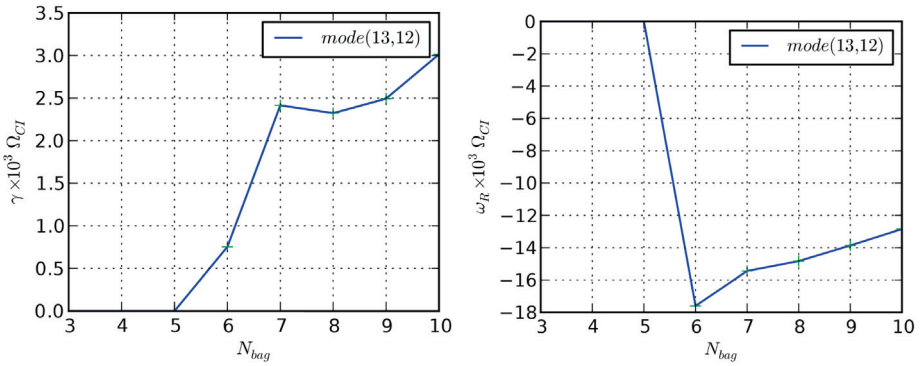

(b) BIG case ; $v_\parallel$ sampling effect for high n modes

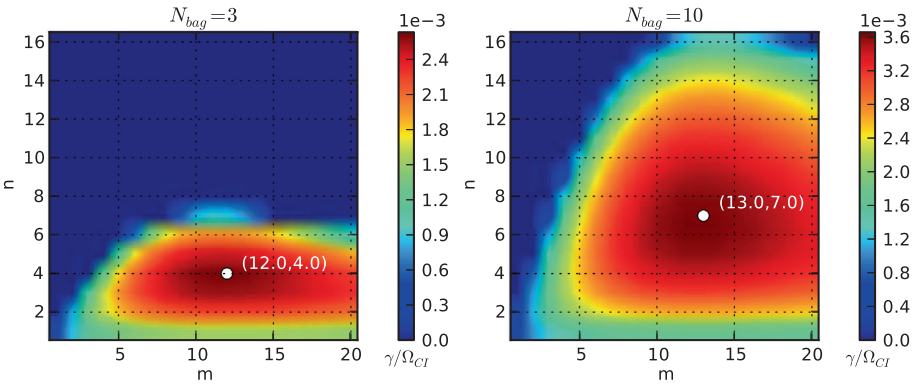

(c) BIG case ; γ maps for 3 and 10 bags respectively

Fig. 6. Pseudo-convergence in N of growth rates and frequencies; $v_\parallel$ sampling effect.

Table 4
SMALL case: Linear and nonlinear eigenvalue solver comparison; growth rates.

(m,n)	γ(NLS)	γ(LS)	Rel error
(8,5)	1.827795073	1.8277951339	−3.33E−008
(9,5)	1.8588793653	1.8588793812	−8.55E−009
(10,5)	1.8715262512	1.8715262519	−3.63E−010
(11,5)	1.8707877033	1.8707876949	4.46E−009
(12,5)	1.8601922576	1.8601922433	7.66E−009
(13,5)	1.8422651104	1.8422650928	9.56E−009

nature of the wave number n. Now if we look more precisely at the effects of bag number variation and $v_\parallel$ sampling, we can confirm what was hinted at in Section 5.1.2. In the bag number range used, there appear to be no clear convergence towards the continuous kinetic result with growing bag number: adding more bags tend to increase the $v_\parallel$ span the of the distribu-

Table 5
SMALL case: linear and nonlinear eigenvalue solver comparison; frequencies.

(m,n)	ω_R(NLS)	ω_R(LS)	Rel error
(8,5)	−5.5108860553	−5.510881896	7.54E−007
(9,5)	−5.5070797926	−5.5070780569	3.15E−007
(10,5)	−5.5073286127	−5.5073279088	1.28E−007
(11,5)	−5.5101623143	−5.5101620336	5.09E−008
(12,5)	−5.51458852	−5.5145884077	2.036E−008
(13,5)	−5.5199428596	−5.5199428125	8.53E−009

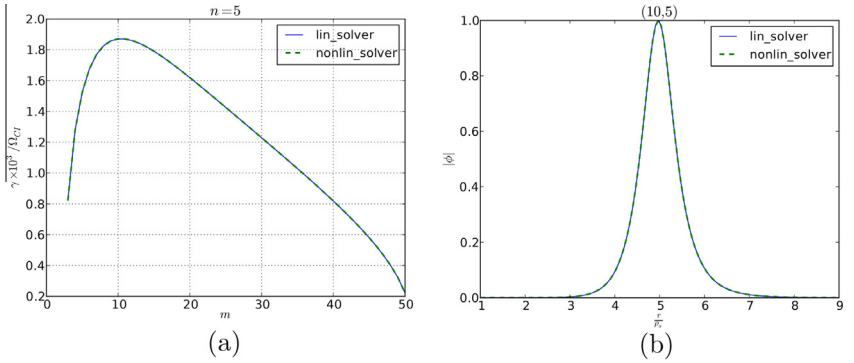

Fig. 7. SMALL case: comparison of linear and nonlinear eigenvalue solvers on growth rates (a) and radial envelopes (b).

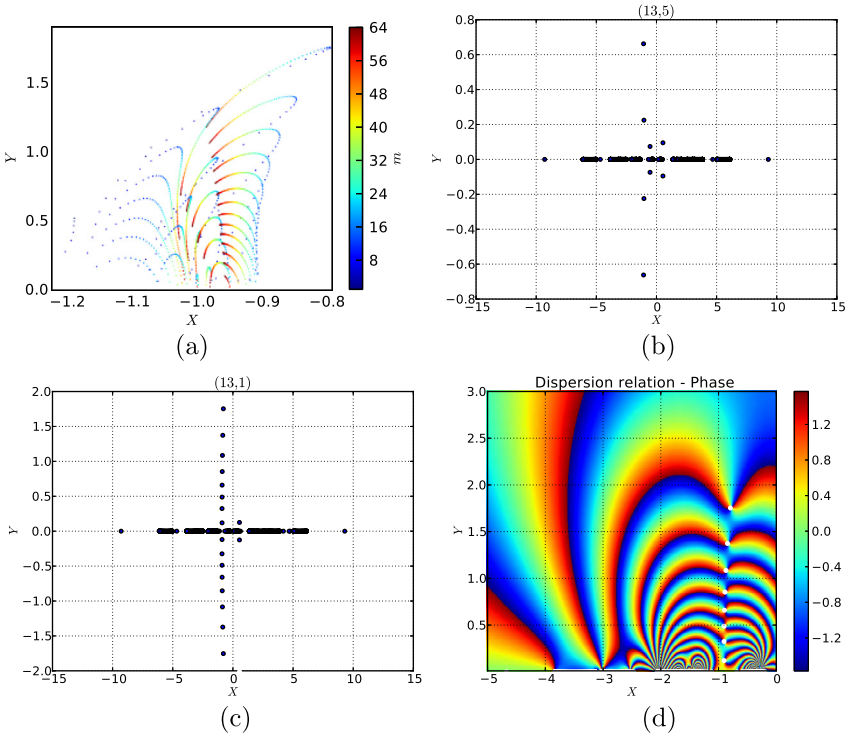

Fig. 8. BIG case: (a) zoom of the full spectrum (all (m,n) values) in the region of interest of the normalized complex frequency plane $X+iY=\frac{\omega}{nk_\parallel}$; (b) spectrum of the most unstable mode $(13,5)$; (c) spectrum of the most unstable mode $(13,1)$; (d) argument of the nonlinear dispersion relation for the $(13,1)$ mode. Linear solver eigenvalues are marked with white dots.

tion, as we cannot pack too many contours in a fixed compact $v_\parallel$ support without violating weights positivity or extensivity constraints. The impact of this modification of $v_\parallel$ extension appears to outweigh the increase of sampling points number, preventing a net decrease in sampling density. This is confirmed by comparing results obtained from two differently

Table 6
Linear and quasilinear cross-validation; growth rates and frequencies normalized to $10^{-3}\Omega_{ci}$; δ indicates relative error; the time range of quasilinear run is $[0, 10000\Omega_{ci}^{-1}]$ with a step $\Delta_t = 20\Omega_{ci}^{-1}$.

Case	Mode	γ_{lin}	γ_{QL}	$\delta\gamma$ (%)	$\omega_{R,lin}$	$\omega_{R,QL}$	$\delta\omega_R$ (%)
SMALL	(6,3)	1.5883	1.6283	2.5	−3.186	−3.1447	−1.3
SMALL	(10,5)	1.8567	1.9142	3.1	−5.214	−5.3461	2.5
MEDIUM	(6,3)	4.4897	4.5756	1.9	−10.5845	−10.6921	1.0
MEDIUM	(10,3)	5.2086	5.2366	0.5	−10.0941	−10.0632	−0.3
BIG	(6,3)	2.6241	2.6407	0.6	−3.2542	−3.1447	−3.4
BIG	(13,5)	3.3111	3.3014	−0.3	−5.3687	-5.3461	−0.4

sampled MWB distributions for a constant number of bags: differences in obtained growth rates can be larger than those obtained when varying the number of bags (Fig. 9). Whether it would be possible to add node constraints allowing to minimize growth rates discrepancies with the continuous case in a generic manner (i.e., independently of the actual values of the initial density and temperature profiles) is still an open question. Nevertheless, considering the low number of $v_\parallel$ sampling points used, the overall agreement between the various MWB models and the continuous Maxwellian model is excellent in the low n region, good around the peaking region, and very node distribution dependent in the high n cutoff region, where sampling artifacts (see e.g., the case of the 6 and 7 bags distributions in Fig. 9 can appear). Relative errors on growth rates range from less than 1% for low n range to a few percent the peaking zone. Error on the cutoff parallel spatial frequency is typically a few (0,1,2) $nk_\parallel$ units but can go up to 5–6 in the worst cases.

5.4.2. Mode envelopes

In the case of a localized gradient zone, global geometry of the most unstable eigenmodes is essentially determined by boundary conditions, the $\left(\frac{m}{r}\right)^2$ centrifugal term, and the Liouville potential $Q(r,\omega)$ in the gradient zone. For those well localized single lobe modes, discrepancies between the various models appear as slight curvature differences, leading to very similar envelopes in modulus, with slight variation in phase (Fig. 10).

5.5. Comparison of global method with a local dispersion relation method using a potential ansatz

The overall robustness to parametric and model variation of mode radial envelope shape in the case of a unique localized gradient zone, could lead to try to solve the linear problem in an even less costly way by taking a reasonable ansatz for the solution electrostatic potential ϕ to obtain a local dispersion relation in the gradient peaking region. This approach is notably used in [3]. Following [3], we use the solution ansatz

$$\phi(r) = \exp\left[-\left(\frac{r-r_0}{\frac{\Delta_{r_n}}{\Delta_{r_T}}}\right)^2\right], \tag{49}$$

which is essentially a Gaussian centered in the peaking η_i region. It should be noted that in order to obtain a local dispersion relation we should a priori provide two complex numbers $d_r^2\phi(r_0)$ and $d_r\phi(r_0)$, up to an arbitrary normalization constant. The choice of (49) amounts to setting $d_r\phi(r_0)$ and $\Im d_r^2\phi(r_0)$ to 0 and setting the curvature of the real part of the mode. In order to compare the results of the local solver of CYLGYR, with the continuous Maxwellian model, with those presented in [3], we use here the previously defined MEDIUM test-case, whose parameters were taken from [3,18]. Results for the local ansatz methods match closely those given in [3]. We then compare results from the local ansatz method and the global solver of CYLGYR on the same test-case. Relative errors between the ansatz method and the non-local solver range in 5–20%. As it can be seen in Fig. 11(c), though the electrostatic potential envelopes are quite close, the sensitivity of the problem both to local modulus curvature and non-zero phase entail large differences in the obtained growth rates. Though the ansatz method has clear computing cost advantages (see Section 5.6), its sensitivity to the quality of the ansatz justifies the added cost of the exact method. Moreover, when the unstable radial regions grow in size or number, or a nonzero average radial electric field is taken into account, the difficulty of finding a reasonable ansatz makes the exact method mandatory.

5.6. Computing costs of the linear solver.

The computing cost of the nonlinear solver scales linearly with radial sampling rate N_r, and in the MWB case with number of bags. On an Intel Xeon W3680, the average cost is about 0.2 ms/$(N_{bag} \times N_r \times N_{modes})$ for a required precision $\epsilon = 10^{-5}nk_\parallel$ and growth rate lower threshold $\gamma_{min} = 10^{-2}nk_\parallel$. Lowering precision to 10^{-8} can increase the cost by a factor 20 to 30 on the same machine. The simple parallelization scheme on (m,n) pairs for a given equilibrium entails loss of parallel efficiency when the number of processes increase towards the number of modes, because of the discrepancy between tasks costs. For typical usage, e.g., studying 1–100 equilibria with 100–300 (m,n) pairs, the loss of efficiency did not justify developing a dynamic parallelization scheme to balance the load between processes. The cost of the linear solver is mostly the one of the

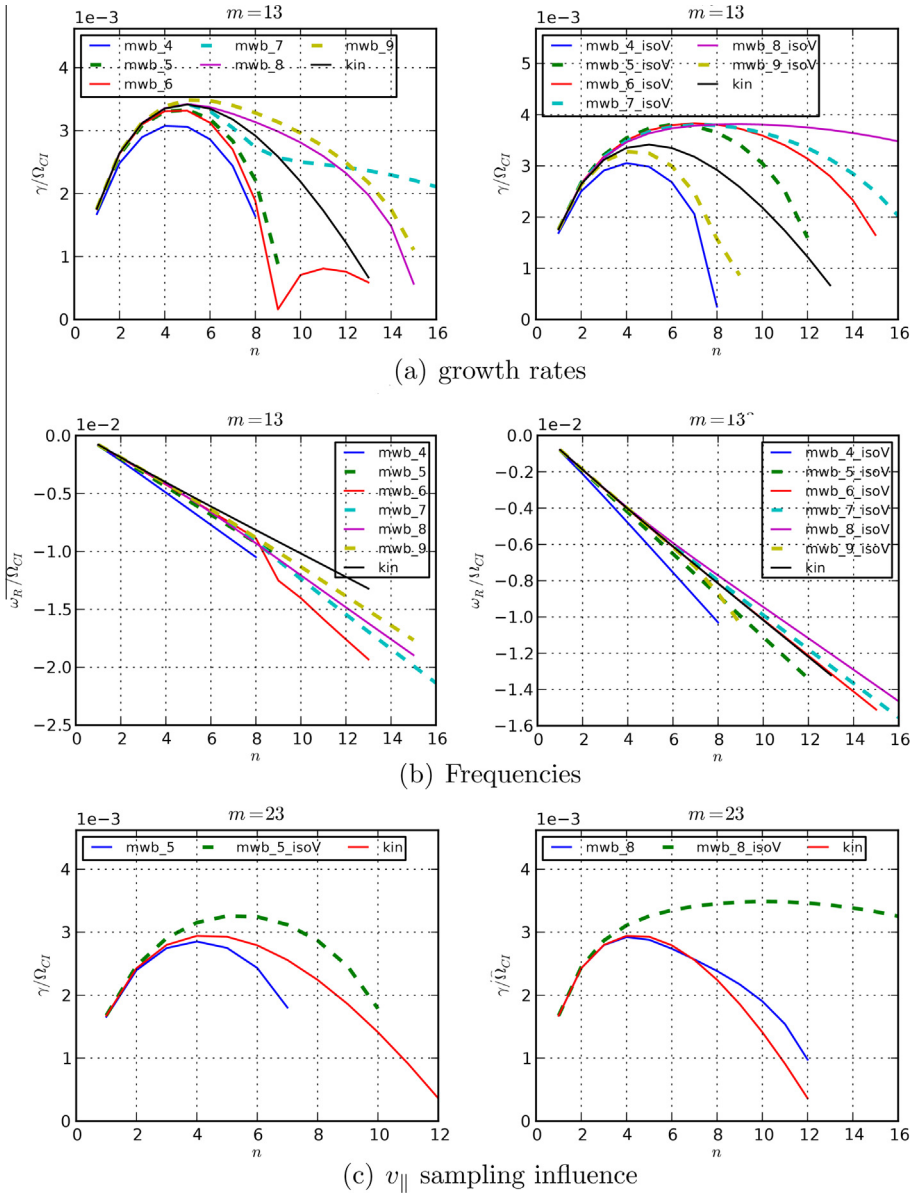

Fig. 9. BIG case: Growth rates (a) and frequency (b) for MWB distributions with equally spaced initial nodes (mwb_N_isoV), non equally-spaced nodes and good radial extensivity (mwb_N) and the continuous Maxwellian model (kin); Influence of bags contours distribution (c).

QZ method implemented in LAPACK, which scales as $N^3 = (2N_{bag} * (N_r - 2))^3$ in computing and memory cost. If one is only interested in the most unstable eigenvalues, the linear method with full QZ factorization is clearly wasteful, as the great majority of computed eigenvalues are discarded. It becomes relevant as a comparison basis for the nonlinear method, and for full spectral studies (see Table 7).

6. Linear, quasilinear and nonlinear code cross-validation.

Once the unstable normal modes for a given equilibrium configuration have been obtained, we can use them to generate perturbations and observe the growth and saturation of the instability using the quasilinear and nonlinear codes. We generate a p-modes perturbation of a scalar field X ($X = v_j, \phi$) of the form

$$\widetilde{X} = \epsilon_{glob} \sum_{q=1}^{p} \epsilon_q X_q(r) \cos\left(m_q \vartheta + n_q k_\parallel z + \alpha_q(r) + \beta_q\right), \tag{50}$$

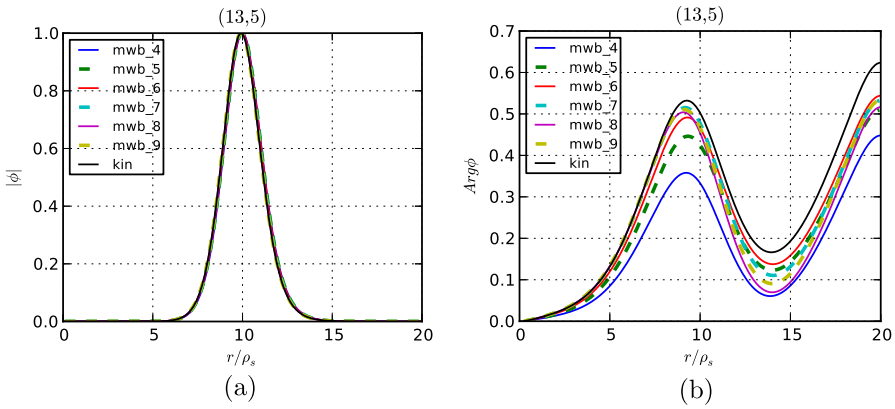

Fig. 10. BIG case: Modulus and phase of the radial envelope of the most unstable mode $(13,5)$.

where ϵ_{glob} sets the perturbation level, ϵ_q allow to weight the various eigenvectors, (X_q, α_q) are the modulus and phase profiles of the qth eigenmode of spectral parameters (m_q, n_q), β_q is a random constant phase factor. Various tests have been performed using 1-mode, 2-modes and many-modes (10 to 300) perturbations. As the various situations share many common features, we focus for clarity purposes on 1-mode perturbations, and precise when results do not apply to multi-modes ones.

6.1. Validation of the linear phase of the nonlinear code.

Initializing the nonlinear code with a low amplitude perturbation ($\epsilon_{glob} = 10^{-6}$) build from an unstable $\phi^n_{mq}(r)$ normal mode, we first check that, in the linear phase, i.e., when the back reaction of the unstable mode growth on the average radial profiles is negligible and after the initial transitory regime, the electrostatic potential Fourier mode $\phi^n_m(r,t)$ is an eigenmode of the discretized nonlinear evolution operator, whose spectral characteristics coincide with those of the linear eigenmode. To that end we have to check that:

- The normalized envelope $\frac{\phi^n_m(r,t)}{\|\phi^n_m\|_\infty(t)}$ is invariant and equals the linear mode one.
- The nonlinear growth rate, evaluated by logarithmic regression on global $(\|\phi^n_m\|_2(t), \|\phi^n_m\|_\infty(t))$, or local $(|\ \phi^n_m\ |\ (r_0,t))$ quantities, equates the linear growth rate. The regression region is determined semi-automatically by optimizing the correlation over a set of time windows, whose position and widths are bounded (see Fig. 12(a)).
- The nonlinear frequency, evaluated by FFT on the time evolution of $\cos(\arg\phi^n_m(r_0,t))$, coincide with the linear ω_r (see Fig. 12(b)).

In the case of 1-mode perturbations, we can also easily check the dynamics of the (0,0) mode in the linear phase, as it takes a particularly simple form. In the linear phase, from (18) where we set $d_r\phi^0_0 = 0$ and $v^n_{jm}(r, t=0) = 0$ we have

$$\Im(\phi^n_m v^{n\star}_{jm}) = -\gamma\ |\ \phi^n_m(\omega,r)|^2 \frac{nk_\parallel - k_\vartheta d_r V^{eq}_j}{(\omega_R - nk_\parallel V^{eq}_j)^2 + \gamma^2} e^{2\gamma t}, \tag{51}$$

where the *eq* superscript implies that quantities keep their equilibrium values. Substituting in (17) we get

$$\partial_t \langle v_\vartheta \rangle_{z,\vartheta} = -2\gamma \frac{m}{rn_0}\ |\ \phi^n_m(\omega,r)|^2 \sum_j A_j \frac{nk_\parallel - k_\vartheta d_r V^{eq}_j}{(\omega_R - nk_\parallel V^{eq}_j)^2 + \gamma^2} e^{2\gamma t}. \tag{52}$$

The (0,0) mode is thus of the form $f(r)\exp(\gamma_{00}t)$ where $f(r)$ is a constant radial envelope and $\gamma_{00} = 2\gamma$. In the multi-mode cases, assuming only one eigenmode per (m,n) pair is used to avoid modulation, integration of (52) yields a combination $\sum_q f_q(r)\exp(2\gamma_q t)$ and thus

$$\phi^0_0(r,t) = f_{qmax}(r) e^{2\gamma_{max}t} \left(1 + \sum_{q\ \neq\ qmax} \frac{f_q}{f_{qmax}} e^{2(\gamma_q - \gamma_{max})t}\right), \tag{53}$$

where $\gamma_{max} = \gamma_{qmax} = \max_q \gamma_q$. The mode growth is dominated by the most unstable mode when $t \gg \sup_{q\ \neq\ qmax} \tau_q$ with

$$\tau_q = \frac{1}{2(\gamma_{max} - \gamma_q)} \ln \left\| \frac{(p-1)f_q}{f_{qmax}} \right\|_\infty. \tag{54}$$

Depending on the number of modes, their relative weights, the values of their growth rates and the duration of the linear phase, we are able to observe a more or less well defined nearly linear growth for the (0,0) mode, whose rate γ_{00} is close to $2\gamma_{max}$.

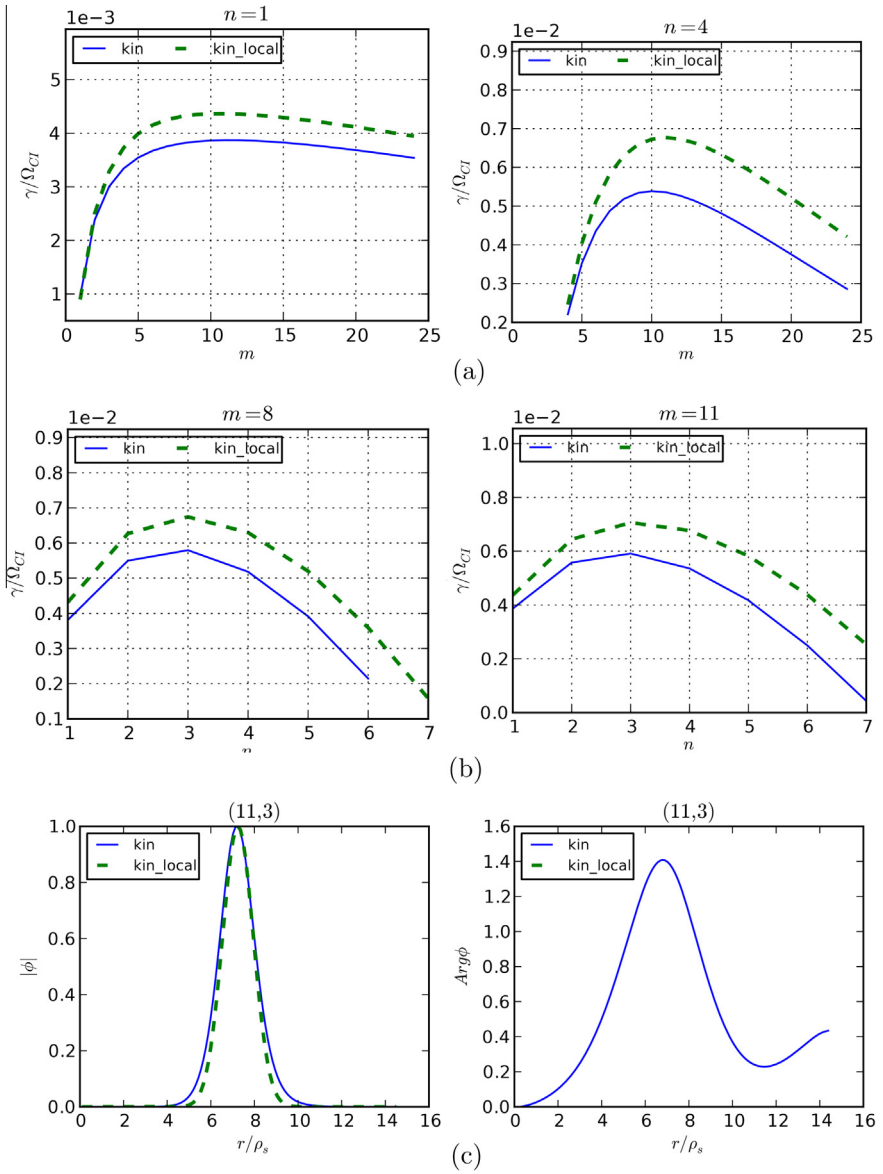

Fig. 11. MEDIUM case: Comparison of the local ansatz and non-local solver results; growth rates (a) and (b), modulus and phase radial profiles (c) (the local ansatz phase is zero on the whole domain).

Table 7
MEDIUM case with nonlinear solver; average runtime per eigenmode $\langle t_{\text{eig}} \rangle$ on Intel XEON 3680 for a $24 \times 8 = 192$ mode map; $N_r = 128$; required precision $\epsilon = 10^{-5} n k_{\parallel}$.

Model	$\langle t_{\text{eig}} \rangle$ (s)
Fluid	0.419
MWB 4	0.833
MWB 6	1.461
MWB 8	2.351
MWB 10	3.337
Kin	84.379
Fluid (local ansatz)	0.0116
Kin (local ansatz)	1.349

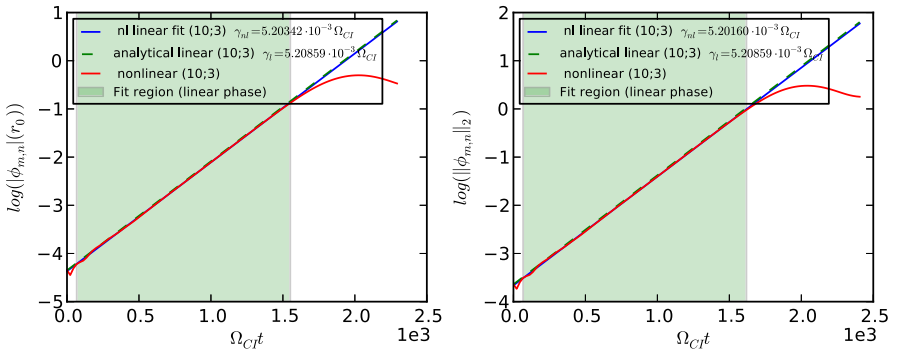

(a) Growth rates estimation by local and non-local regression

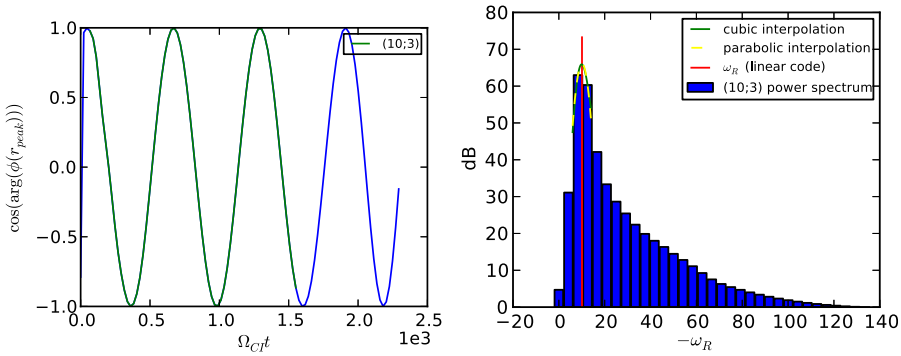

(b) Frequency estimation by peak detection on time power spectrum

Fig. 12. MEDIUM case perturbed by $(10,3)$: temporal characteristics computation in the linear phase of the nonlinear code; the time window used to compute the spectrum in (b) (green colored part of the signal) is obtained from the optimal linear regression region computed in (a); refined peak frequency is obtained by local parabolic or cubic interpolation around the on-grid peak frequency. (For interpretation of the references to colour in this figure caption, the reader is referred to the web version of this article.)

Table 8
1 mode perturbations: growth rates; γ_{nl} is estimated by regression on $\|\phi\|_2$; δ is the relative error between linear and non linear perturbation growth rate; δ_{00} and δ'_{00} are the relative errors between (0,0) mode growth rate γ_{00} and respectively $2\gamma_{\text{lin}}$ and $2\gamma_{\text{NL}}$; frequencies are expressed in $10^{-3}\Omega_{\text{CI}}$ units.

CASE	Mode	γ_{lin}	γ_{nl}	δ (%)	γ_{00}	δ_{00} (%)	δ'_{00} (%)
SMALL	(6,3)	1.588	1.572	−1.05	3.147	−0.9	0.1
SMALL	(10,5)	1.872	1.885	0.7	3.674	−1.9	−2.5
MEDIUM	(6,3)	4.490	4.486	−0.07	8.905	−0.8	−0.7
MEDIUM	(10,3)	5.209	5.193	−0.3	10.347	−0.7	−0.4
BIG	(6,3)	2.624	2.615	−0.4	5.076	−3.3	−2.9
BIG	(13,5)	3.311	3.502	5.7	7.132	7.7	1.8

Table 9
One mode perturbations: frequencies; ω_{max}: on-grid peak frequency; $\Delta\omega$: grid resolution; ω_{parab}: peak frequency obtained by parabolic interpolation; δ_{parab}: relative error with ω_{lin}; frequencies are expressed in $10^{-3}\Omega_{\text{CI}}$ units.

Cas	Mode	ω_{lin}	ω_{max}	$\Delta\omega$	ω_{parab}	δ_{parab} (%)
SMALL	(6,3)	−3.18630420404	−3.35103216383	0.837758040957	−3.01482138131	−5.38187228056
SMALL	(10,5)	−5.50732861185	−5.74462656656	0.957437761094	−5.53064334202	0.423340094913
MEDIUM	(6,3)	−10.5844754066	−9.863861734	1.64397695567	−10.2807017471	−2.86999258692
MEDIUM	(10,3)	−10.0941370698	−8.34256962577	2.08564240644	−10.1044493346	0.102160935
BIG	(6,3)	−3.25420476447	−3.82975104438	0.957437761094	−3.32344644396	2.12776037458
BIG	(13,5)	−5.36868314324	−5.36165146213	1.34041286553	−5.33804671893	−0.570650632441

6.1.1. Growth rates and frequencies in the linear phase

We observe a good agreement between nonlinear and linear growth rates, with relative error typically around 1%, and up to 5% among the various perturbations tested. For 1-mode perturbations, linear growth of the (0,0) mode with rate $\gamma_{00} = 2\gamma$

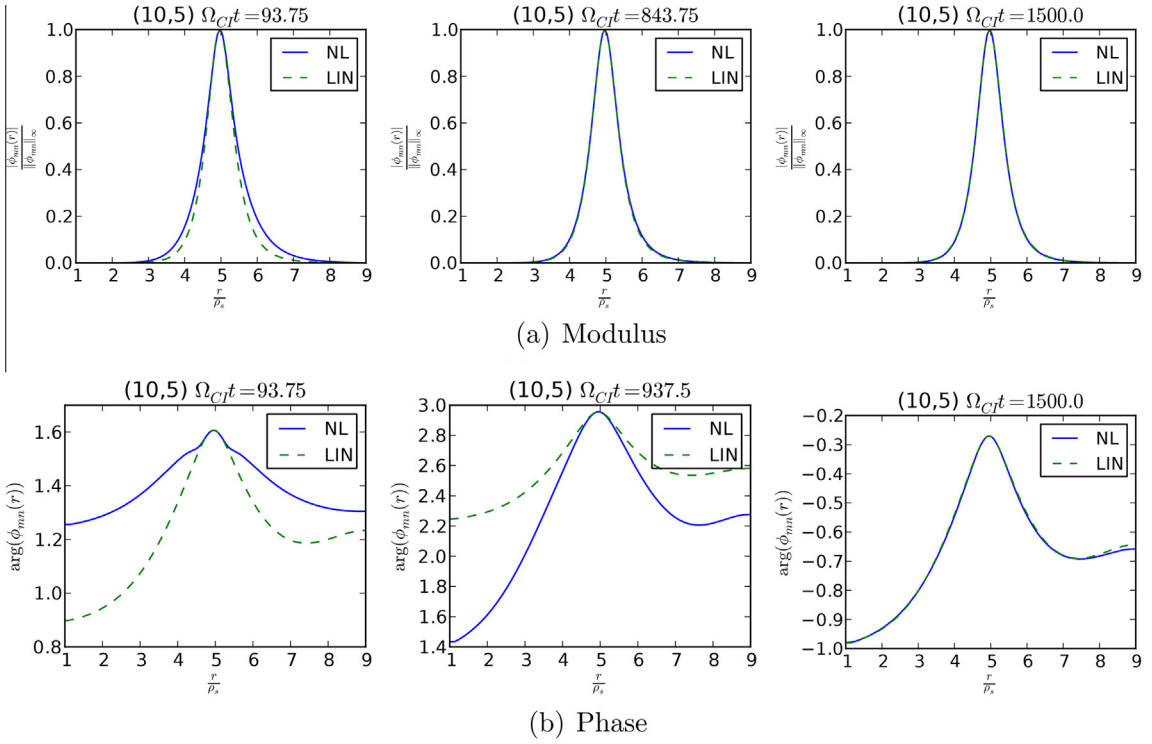

Fig. 13. SMALL case: 1-mode perturbation; snapshots of envelope evolution in the linear phase; envelopes match perfectly at $t = 0$ (not shown); the maximum transient distortion is at $t = 93,75\Omega_{CI}^{-1}$; modulus locks back earlier at $t = 843\Omega_{CI}^{-1}$ than phase ($t = 1500\Omega_{CI}^{-1}$.)

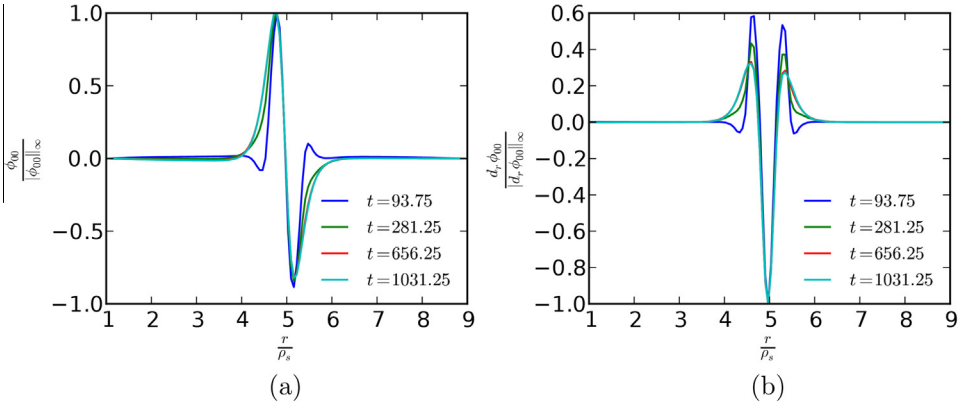

Fig. 14. SMALL case: 1-mode perturbation by $(10, 5)$; evolution of normalized (z, ϑ)-averaged electrostatic potential (a) and mean poloidal drift velocity (b) radial envelopes in the early linear phase.

is confirmed within a few percent relative error. Table 8 shows result samples for the 1-mode perturbations. In the case of mode baths, the least unstable modes can be prevented from having a linear phase: their initial transient phase is longer but the saturation is driven through the (0,0) mode level by the most unstable modes, voiding the linear phase time range. For all modes unstable enough to have a well defined linear growth phase, relative errors stays of the same order as in the 1-mode cases. Keeping in mind that frequency estimation is limited by the small number of periods in the linear phase (typically 2–3), good agreement is also observed between estimated nonlinear frequencies and linear ones: absolute errors are always below frequency grid resolution, and relative error between the interpolated (see Fig. 12(b)) peak frequency and the linear one is a few percent at most (see Table 9).

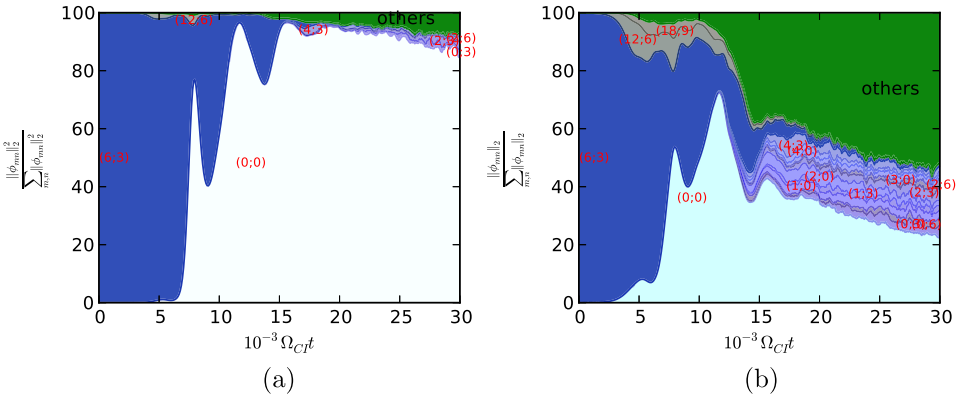

Fig. 15. SMALL case perturbed by (6,3): dominant modes in electric potential power spectrum; $\|\cdot\|_2^2$ ratios (a); $\|\cdot\|_2$ ratios (b); sorting threshold is 2% in both cases.

6.1.2. Radial envelopes in the linear phase

Envelope geometry is examined through direct observation of modulus and phase radial profiles (Fig. 13) and quantitative synthetic characteristics parameters as was done in Section 5.3. Behavior is the same in all test-cases observed: during the initial transient, a slight distortion of the envelope appears, then the mode locks back to the linear envelope during the linear phase, with faster lock back in normalized modulus than in phase. Average relative error on normalized modulus envelope peaks at a few percent during the transient, then stays well below 1% during the linear phase. The (z,ϑ) average electrostatic potential ϕ_0^0 envelope of the nonlinear code converges during the transient (early linear phase) to its linear phase asymptotic profile, as predicted by (52). After this initial convergence has occured, normalized envelope variation stays negligible during the linear growth phase. Fig. 14 shows the potential envelope and the resulting poloidal velocity shear flow at key instants in the early linear phase in the case of a 1-mode perturbation.

6.2. Overview of nonlinear spectral dynamics: synthetic diagnostics

As soon as the perturbation grows, the quadratic coupling terms of (13) give birth to spectrum broadening in the (m,n) spectral plane. Observing the power spectra evolution with time can give a good idea of the dynamics of the harmonic cascades, but does not provide a synthetic overview of the spectral evolution over the whole simulation time range. In order to obtain a synthetic representation of the time evolution of the spectral contents, we compute at each time t_i the relative weights of individual modes in radial norm $\|.\|_2^2$ (normalized power spectrum) and $\|.\|_2$, the latter allowing one to enhance low level mode representation. All modes whose relative weight is above a fixed threshold at some point in time are explicitly represented, while the others are binned together. Such a representation is shown in Fig. 15 for the SMALL case, perturbed by a single (6,3)-mode. The (6,3)-mode dominates the spectrum in the initial linear phase. nonlinear couplings then lead simultaneously to generation on one hand of the strongly dominating (0,0) zonal flow, and higher harmonics (12,6) and (18,9) of the initial perturbation. During that phase, we observe oscillations of the (6,3)-mode and the mean gradients (Fig. 18). Relaxation of the initial unstable equilibrium to the final marginally stable state does not occur in one run but though intermediary marginally stable states (Fig. 17). This oscillating behavior is extremal in 1-mode perturbation where strong feedback coupling exists between the perturbed mode and the (0,0)-flow. In multi-mode perturbations, oscillations amplitude decreases as the number of perturbed modes increases, leading to a direct relaxation for large numbers of modes. In all cases, the spectrum tends afterward to a continuous one, since more and more harmonics are generated, strongly dominated by the (0,0)-flow. In order to give a more direct picture of the perturbation evolution, perturbed density snapshots for a 1-mode perturbation scenario are shown in Fig. 16. After initial growth of the unstable mode, we observe a shearing and tearing of the convective cells, apparition of smaller sized structures and dominance of the zonal flow at the end of simulation. Global evolution of the $k_\perp$ spectrum is obtained by performing discrete Hankel tranforms on (m,n) mode radial profiles, avoiding the need for polar to Cartesian grid interpolation. We can then follow the time evolution of the $k_\perp$ spectra. As the simulation scenario is one of relaxation, no steady-state spectrum can be expected to appear like in statistically stationary turbulence scenarii with forcing or sustained energy injection at some chosen scales. We can nevertheless observe relaxation to spectra exhibiting power-law tails, as can be seen in Fig. 19.

6.3. Nonlinear, quasilinear and linear cross comparisons during first saturation

After the initial transient, the linear growth phase of the perturbation lasts until the (0,0) mode perturbation is strong enough to make the eigenstructure computed from equilibrium fields unable to represent accurately the perturbed mode growth. Supposing we know the state of the (0,0) fields at time t_i, we can compute the eigenstructure of the linear problem

corresponding to the initial value problem starting at time t_i, considering the (0,0) fields frozen for time $t > t_i$. Let us recall that this "adiabatic" linear model does not take into account the time variation of the (0,0) fields, reducing the convolution products appearing in the Fourier–Laplace transform of (15) to mere products in (18). It is however meant to provide an insight on the stability properties of the system state at time t_i. Now, as the eigenspaces computed at time t_i and t_{i+1} are different, the projection of a single eigenmode of the t_i state on the t_{i+1} eigenspace spans in general several eigenmodes. When we consider only the most unstable normal mode for a given (m, n) pair, this spectral spreading leads to an additional loss of accuracy in the representation of the dynamical state. Divergence of this "1-eigenmode" adiabatic linear model with the nonlinear evolution happens for the two aforementioned reasons, even when the dynamics is dominated by couplings with the (0,0) mode. Divergence of the quasilinear model forced by the (0,0) fields of the nonlinear one and the nonlinear model

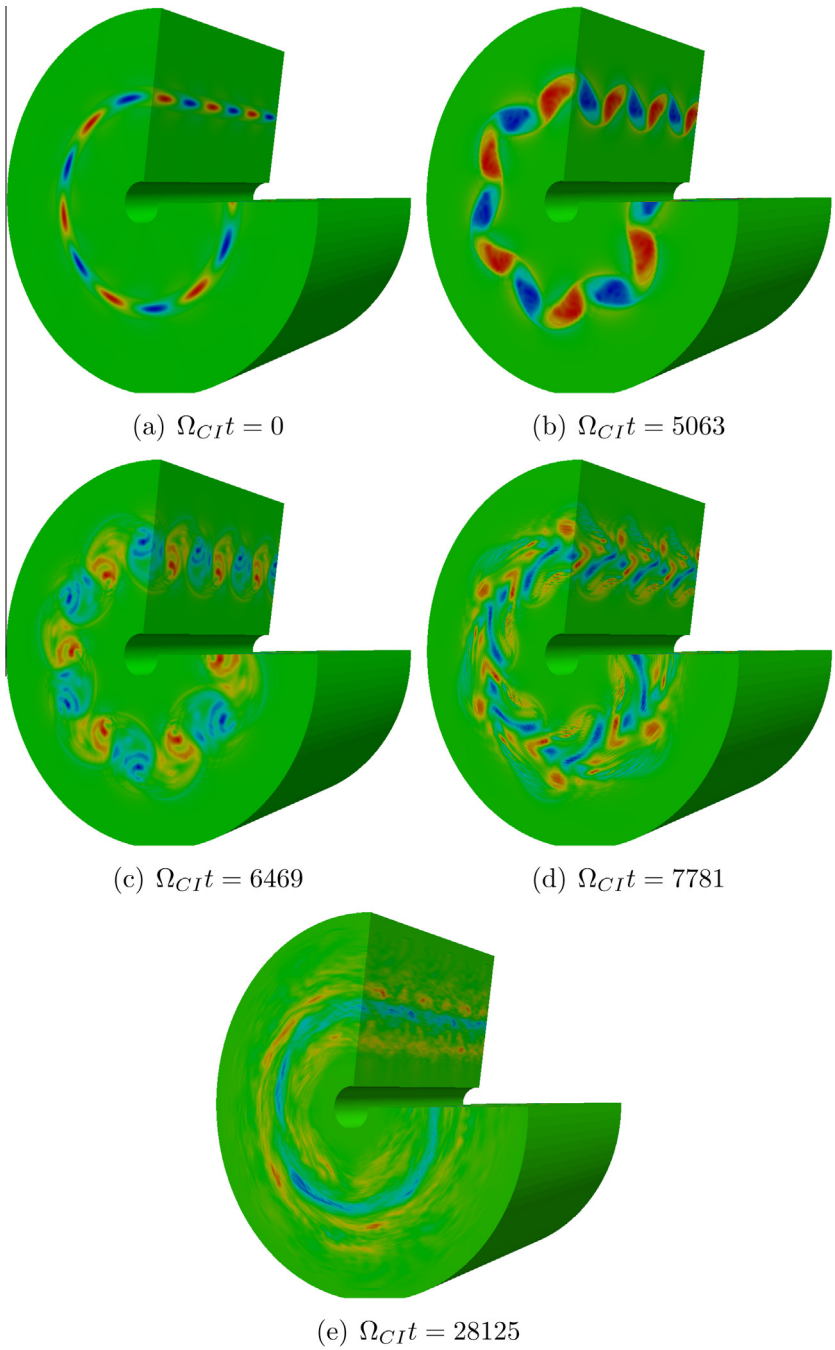

Fig. 16. SMALL perturbed by (6,3); density perturbation snapshots

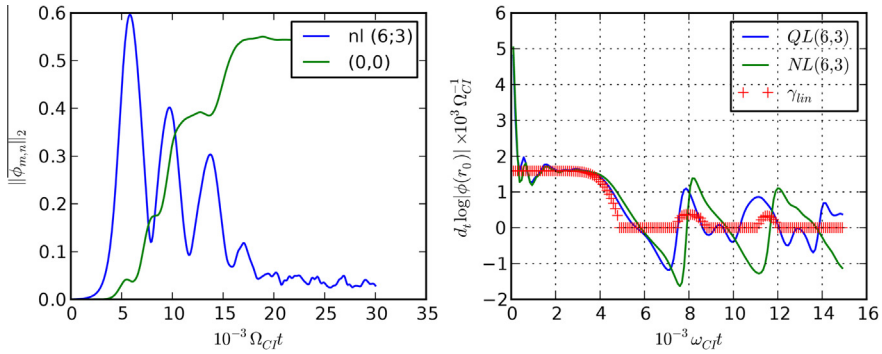

Fig. 17. SMALL case perturbed by (6,3): multi-stages relaxation to marginal stability; (6,3) and (0,0) modes evolution (left); estimated grow rates for the three dynamical models (right).

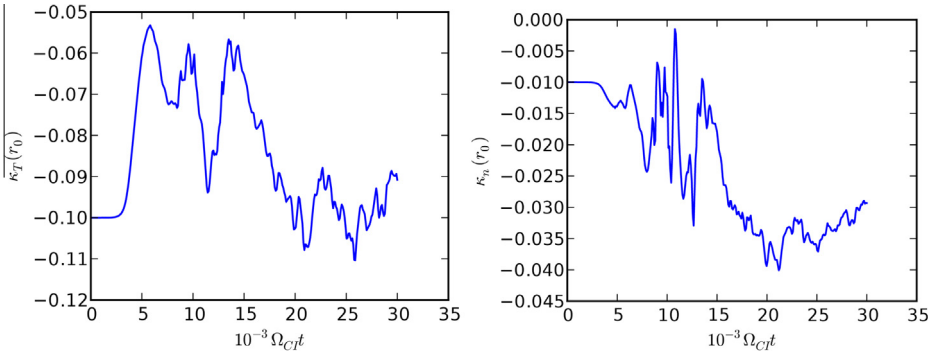

Fig. 18. SMALL case perturbed by (6,3): multi-stages relaxation to marginally stable state; mid-radius temperature (left) and density (right) normalized gradients oscillations.

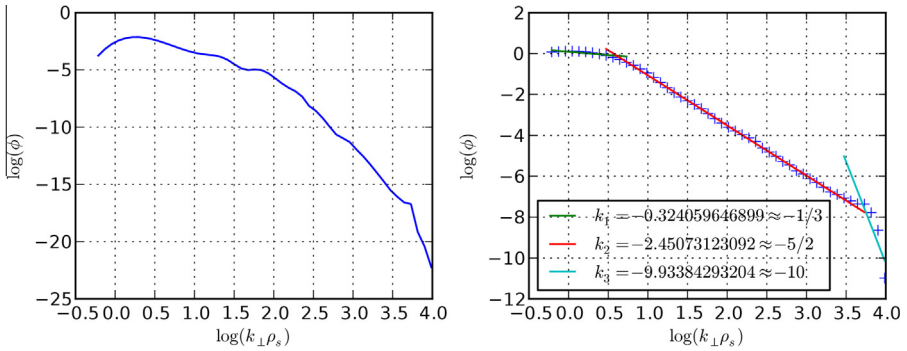

Fig. 19. SMALL case perturbed by (6,3): $k_\perp$ spectra of electrostatic potential at $\Omega_{CI}t = 3750$ in the linear phase (left) and at $\Omega_{CI}t = 30,000$ (right).

occurs when the effect of the nonlinear cascade become non-negligible. In order to examine model divergence during the first stages of saturation, we follow the time evolution of three quantities: the linear growth rate of the most unstable mode (for given (m,n) parameters) and the logarithmic derivative of a functional of the mode envelope ($\|\phi\|_2, \|\phi\|_\infty, |\,\phi(r_0)\,|$) for the quasilinear and nonlinear model. The three quantities are equal in the linear phase (after oscillations during the initial transient). For 1-mode perturbations (Fig. 20), we observe a good fit of the forced quasilinear and nonlinear models up to the first saturation. As expected, the linear growth rates anticipates the saturation dynamics of the two other models: the linear model underestimates the first saturation time (first cancellation of γ). Conversely, the linear instability threshold is overestimated.

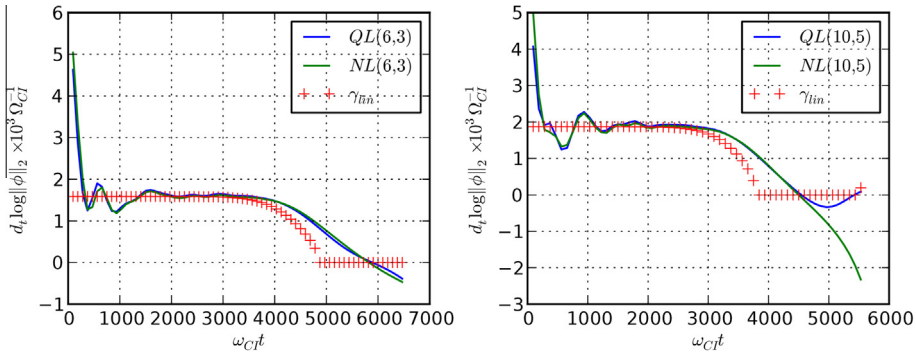

Fig. 20. SMALL case; 1-mode perturbations: pseudo growth rates comparison in the linear and first saturation phase for the nonlinear (NL), forced quasilinear (QL) and adiabatic linear models.

7. Conclusions and prospects

For all combinations of test-cases and perturbations studied, the linear, quasilinear and nonlinear models show good numerical agreement in the linear growth phase of the instability, for both temporal and geometric properties of the unstable modes, establishing the consistency of the three multi-water-bag models implemented. Comparison of linear normal modes between the multi-water-bag and continuous Maxwellian models show that quantitative agreement can be reached with low number of bags distributions for part of the spectrum. Further improvements in the multi-water-bag parameters setting scheme are however needed to allow for a better control of $v_\parallel$ sampling to ensure optimal convergence of the multi-water-bag model to the continuous one when increasing the number of bags. Moreover, application of the multi-water bag model to fusion relevant domain sizes and magnetic field geometry in a gyrokinetic framework is underway, which will allow meaningful comparisons with advanced gyrokinetic codes.

Appendix A. Explicit inversion of Vandermonde system

Consider a generic Vandermonde system, of distinct positives nodes C_j, defined for $0 \leqslant p \leqslant N-1$ by

$$\sum_{j=1}^{N} X_j C_j^p = Y_p, \tag{A.1}$$

or in matrix form

$$\mathcal{C}X = Y, \tag{A.2}$$

where $C_{pj} = C_j^p$. The Lagrange interpolation polynomial $\mathcal{L}_j(Z)$ on the nodes $C_k, j \neq k$ is defined as

$$\mathcal{L}_j(Z) = \frac{\prod_{k\neq j}(Z - C_k)}{\prod_{k\neq j}(C_j - C_k)} = \sum_{p=0}^{N-1} \lambda_{jp} Z^p. \tag{A.3}$$

From the interpolation property of $\mathcal{L}_j(Z)$ and since $C_{pj} = C_j^p$ we get

$$\sum_k \sum_p \lambda_{jp} C_{pk} = \sum_k \sum_p \lambda_{jp} C_k^p = \sum_k \mathcal{L}_j(C_k) = \delta_{kj}. \tag{A.4}$$

The inverse of $\mathcal{C}$ is thus the matrix whose jth row contains the polynomial coefficients of $\mathcal{L}_j$. Solution of system (A.1) then reads

$$\forall j, X_j = \sum_p \lambda_{jp} Y_p. \tag{A.5}$$

In the case of moment equivalence we have $X_j = A_j V_j, C_j = V_j^2, Y_p = \mathcal{M}_{2p}^M$ and the expression for the weights become

$$A_j = \frac{1}{V_j} \sum_p \lambda_{jp} \mathcal{M}_{2p}^M. \tag{A.6}$$

Appendix B. Conditions for positivity of weights

As shown in Appendix A, the weights A_j of a multi-water-bag distribution with N bags satisfying exact moment equivalence for N even moments can be expressed as functions of the reference moments and the coefficients of the Lagrange

interpolation polynomials on the subsets $V_k^2, k \neq j$. Let us note $\sigma_p(X_1, X_2, \ldots, X_{N-1})$ the pth symmetric polynomial and $\sigma_{jp} := \sigma_p(X_1 = V_{j_1}, X_2 = V_{j_2}, \ldots, X_{N-1} = V_{j_{N-1}})$ where $j_1, j_2, \ldots, j_{N-1} \neq j$. We then have

$$\prod_{k \neq j}(Z + V_k^2) = \sum_{p=0}^{N-1} \sigma_{jp} Z^p. \tag{B.1}$$

The Lagrange interpolation polynomial coefficient λ_{jp} can be rewritten as

$$\lambda_{jp} = \frac{(-1)^{N+p-1}\sigma_{jp}}{\prod_{k \neq j}(V_j^2 - V_k^2)}. \tag{B.2}$$

Taking into account the ordering $V_1 < V_2 < \cdots < V_N$, the sign of the denominator is $(-1)^{N-j}$ and the condition $A_j > 0$ can be expressed as

$$(-1)^j \sum_{p=0}^{N-1} (-1)^{p-1} \sigma_{jp} \mathcal{M}_{2p}^M > 0. \tag{B.3}$$

Let us define the $N-1$ variables multivariate symmetric polynomial $S = \sum_p (-1)^{p-1} \sigma_p \mathcal{M}_{2p}$. Let us define $\mathcal{V}^{+1}, \mathcal{V}^{-1}, \mathcal{V}^0$ the manifolds of $(\mathbb{R}^{+*})^{N-1}$ where S is respectively positive, negative and zero. For all j we note W_j the point of $(\mathbb{R}^{+*})^{N-1}$ defined by the ordered $V_k, k \neq j$. The weight positivity condition can be rewritten as

$$\forall j, W_j \in \mathcal{V}^{(-1)^j}. \tag{B.4}$$

Now lets consider $j' > j$ of different parity. Taking into account the invariance of S by any permutation of variables in $(\mathbb{R}^{+*})^{N-1}$, we can deduce from (B.4) that there must exist $\alpha_{jj'}$ such that

$$V_j^2 < \alpha_{jj'} < V_{j'}^2 \text{ and } \left(\alpha_{jj'}, \left\{V_k^2, k \neq j, j'\right\}\right) \in \mathcal{V}^0 \tag{B.5}$$

To make the above property clearer, let us consider an example with $N = 4$. The weights positivity constraints become

$$S(V_2^2, V_3^2, V_4^2) < 0, \tag{B.6}$$

$$S(V_1^2, V_3^2, V_4^2) > 0, \tag{B.7}$$

$$S(V_1^2, V_2^2, V_4^2) < 0, \tag{B.8}$$

$$S(V_1^2, V_2^2, V_3^2) > 0. \tag{B.9}$$

From (B.6) and (B.7), we deduce the existence of a root α_{12} of $S(X, V_3^2, V_4^2)$ between V_1^2 and V_2^2. From (B.7) and (B.8), we can deduce the existence of a root α_{23} of $S(V_1^2, Y, V_4^2)$ which we can recast by symmetry of S as a root α_{23} of $S(X, V_1^2, V_4^2)$. Combining the other inequalities this way we deduce the necessary existence of four positive real numbers $\alpha_{12}, \alpha_{12}, \alpha_{14}, \alpha_{23}, \alpha_{34}$ such that

$$V_1^2 < \alpha_{12} < V_2^2 \text{ and } (\alpha_{12}, V_3^2, V_4^2) \in \mathcal{V}^0, \tag{B.10}$$

$$V_1^2 < \alpha_{14} < V_4^2 \text{ and } (\alpha_{14}, V_2^2, V_3^2) \in \mathcal{V}^0, \tag{B.11}$$

$$V_2^2 < \alpha_{23} < V_3^2 \text{ and } (\alpha_{23}, V_1^2, V_4^2) \in \mathcal{V}^0, \tag{B.12}$$

$$V_3^2 < \alpha_{34} < V_4^2 \text{ and } (\alpha_{12}, V_1^2, V_2^2) \in \mathcal{V}^0, \tag{B.13}$$

Obtaining explicit criteria for weights positivity from condition (B.5) would require a complete characterization of the manifold $\mathcal{V}^0$, which is out of the scope of the present work.

We can nonetheless obtain necessary conditions for the extreme nodes V_1, V_N from the initial system. Taking any two exact equivalence equations at orders $2p$ and $2q$, dividing by the reference moment and taking the difference we obtain

$$\sum_j A_j \left(\frac{V_j^{2p+1}}{\mathcal{M}_{2p}^M} - \frac{V_j^{2q+1}}{\mathcal{M}_{2q}^M}\right) = \sum_j A_j \frac{V_j^{2q+1}}{\mathcal{M}_{2p}^M}\left(V_j^{2(p-q)} - \frac{\mathcal{M}_{2p}^M}{\mathcal{M}_{2q}^M}\right) = 0. \tag{B.14}$$

Assuming that $A_j > 0$ for all j we deduce that for all $(p, q) \in [1, N]^2$, there exist j_1, j_2 such that

$$V_{j_1} < \left(\frac{\mathcal{M}_{2p}^M}{\mathcal{M}_{2q}^M}\right)^{\frac{1}{2(p-q)}} < V_{j_2}. \tag{B.15}$$

Taking into account the ordering $V_1 < V_2 < \cdots < V_N$ we obtain necessary conditions on the extreme nodes

$$V_1 < \min_{p,q}\left(\frac{\mathcal{M}^M_{2p}}{\mathcal{M}^M_{2q}}\right)^{\frac{1}{2(p-q)}}, \tag{B.16}$$

$$V_N > \max_{p,q}\left(\frac{\mathcal{M}^M_{2p}}{\mathcal{M}^M_{2q}}\right)^{\frac{1}{2(p-q)}}. \tag{B.17}$$

Appendix C. Non-local extensibility conditions for MWB exact moment equivalence

In this part we show that MWB moments obey general inequalities relying only on MWB structure and bearing no dependence on the target moments used for moment equivalence. When trying to build an MWB distribution by exact moment equivalence, these inequalities are transferred to the target moments and thus limit the equivalence domain to the target moment subspace satisfying said inequalities. The restriction on accessible moments, through spatial moments dependency, restricts the spatial extensibility of moment equivalence. Let us recall that the expression for the $2p$th order MWB moment for a symmetric distribution is

$$\mathcal{M}^{MWB}_{2p} = \sum_{j=1}^{N} 2A_j \frac{V_j^{2p+1}}{2p+1}, \tag{C.1}$$

where $A_j > 0$, $V_j > 0$. Capital notation for the V_j emphasizes the fact that we are not considering here the V_j as functions of space, but the even moments as function of the positive $V_j, j \in [1, N]$, viewed as points of $\mathbb{R}^N$. Accordingly, the default range of summation on bag index j is from 1 to N. To clarify notations note $A = (A_1, A_2, \ldots, A_N) \in (\mathbb{R}^{+*})^N$ and $V = (V_1, V_1, \ldots, V_N) \in \mathbb{R}^N$. To avoid confusions with coordinates, we use exponent notation (e.g. $V^{(i)}$) when indexing points of $\mathbb{R}^N$.

C.1. General MWB moments inequality

$A \in (\mathbb{R}^{+*})^N$ being given, we define the mapping $\mathcal{L}_{p,A} : \mathbb{R}^N \to \mathbb{R}^+$ by

$$\mathcal{L}_{p,A}(V) = \left(\mathcal{M}^{MWB}_{2p}\right)^{\frac{1}{2p+1}} = \left(\sum_j 2A_j \frac{V_j^{2p+1}}{2p+1}\right)^{\frac{1}{2p+1}}. \tag{C.2}$$

For all $p \in \mathbb{N}^{\star}$, $\mathcal{L}_{p,A}$ defines a weighted $2p+1$-norm on $\mathbb{R}^N$. All norms being equivalent on $\mathbb{R}^N$, we deduce that for all $(p,q) \in \mathbb{N}^2$ such that $p \neq q$ there exist $(m_{A,p,q}, M_{A,p,q}) \in (\mathbb{R}^{+*})^2$ satisfying for all $V \in \mathbb{R}^N$ the inequalities

$$m_{A,p,q}\mathcal{L}_{q,A}(V) < \mathcal{L}_{p,A}(V) < M_{A,p,q}\mathcal{L}_{q,A}(V), \tag{C.3}$$

from which we derive the general condition on MWB moments

$$m^{2p+1}_{A,p,q}\left(\mathcal{M}^{MWB}_{2q}\right)^{\frac{2p+1}{2q+1}} < \mathcal{M}^{MWB}_{2p} < M^{2p+1}_{A,p,q}\left(\mathcal{M}^{MWB}_{2q}\right)^{\frac{2p+1}{2q+1}}. \tag{C.4}$$

C.2. Explicit bounds

C.2.1. General properties

Condition (C.4) cannot provide useful bounds, as it does not take into account restrictions on the accessible V space. We now derive slightly more restrictive conditions, taking into account constraints on admissible V, by adding control parameters on nodes support and minimum inter-contour distance. We first build from (C.4) a family of functions whose extremal values provide the requested bounds using standard optimization techniques.

Definition 1. From (C.4) we define on $(\mathbb{R}^{+*})^N$ the mapping $\mathcal{F}_{A,p,q}$ by

$$\mathcal{F}_{A,p,q}(V) := \left(\frac{\mathcal{L}_{p,A}(V)}{\mathcal{L}_{q,A}(V)}\right)^{(2p+1)(2q+1)} = \frac{(q+\frac{1}{2})^{2p+1}}{(p+\frac{1}{2})^{2q+1}} \frac{\left(\sum_j A_j V_j^{2p+1}\right)^{2q+1}}{\left(\sum_j A_j V_j^{2q+1}\right)^{2p+1}}. \tag{C.5}$$

The bounding parameters we seek are the bounds of $\mathcal{F}$ on a properly defined subspace of $(\mathbb{R}^{+*})^N$. As $\mathcal{F}_{A,p,q} = \frac{1}{\mathcal{F}_{A,q,p}}$, we can without loss of generality consider restrict the study to $q > p$. The $p > q$ cases can be recovered by mere inversion of inequalities.

Property 1. Functions $\mathcal{F}_{A,p,q}$ are scale invariant (homogenous of 0th degree). For all (p,q) such that $p \neq q$ and for all $\lambda \in \mathbb{R}^*$ we have

$$\mathcal{F}_{A,p,q}(\lambda V) = \mathcal{F}_{A,p,q}(V). \tag{C.6}$$

A corollary of the previous statement is that for all V

$$V \cdot \nabla \mathcal{F}_{A,p,q}(V) = 0. \tag{C.7}$$

Property 2. For all $k \in [1, N]$

$$\frac{\partial \mathcal{F}_{A,p,q}}{\partial V_k} = 0 \Longleftrightarrow V_k = \left(\frac{\Sigma_q}{\Sigma_p}\right)^{\frac{1}{2(q-p)}}, \tag{C.8}$$

where $\Sigma_i := \sum_{j=1}^{N} A_j V_j^{2i+1}, i = p, q$.

Proof

$$\frac{1}{\mathcal{F}_{A,p,q}} \frac{\partial \mathcal{F}_{A,p,q}}{\partial V_k} = (2p+1)(2q+1) A_k \left(\frac{V_k^{2p}}{\Sigma_p} - \frac{V_k^{2q}}{\Sigma_q}\right). \tag{C.9}$$

Taking into account that $\mathcal{F}_{A,p,q} \neq 0$ and $V \in (\mathbb{R}^{+*})^N$ we have

$$\frac{\partial \mathcal{F}_{A,p,q}}{\partial V_k} = 0 \Longleftrightarrow V_k = \left(\frac{\Sigma_q}{\Sigma_p}\right)^{\frac{1}{2(q-p)}}. \qquad \square \tag{C.10}$$

From the previous property and the form of the gradient components we deduce the following properties.

Property 3. Let $V \in (\mathbb{R}^{+*})^N$ and $1 \leqslant j, j' \leqslant N$. The following properties hold.

$$\begin{aligned} &\text{If } (\nabla \mathcal{F}_{A,p,q})_j > 0 \quad \text{and} \quad (\nabla \mathcal{F}_{A,p,q})_{j'} < 0 \quad V_{j'} > V_j, \\ &\text{If } (\nabla \mathcal{F}_{A,p,q})_j = 0 \quad \text{and} \quad (\nabla \mathcal{F}_{A,p,q})_{j'} = 0 \quad V_{j'} = V_j. \end{aligned} \tag{C.11}$$

In the case $q < p$ the ordering in the first statement is reversed.

Property 4. Let $V \in (\mathbb{R}^{+*})^N$.

$$\mathcal{F}_{a,p,q}(V) = 0 \Longleftrightarrow V \in span[1, 1, \ldots, 1] \cap (\mathbb{R}^{+*})^N. \tag{C.12}$$

Proof. Canceling condition of the kth component of the gradient implies that V_k takes a value independent of k. If $N > 1$, the gradient can only cancel if $V_k = V'_k, \forall k, k'$, i.e., on the one-dimensional subspace spanned by $[1, 1, 1, \ldots, 1]$, where all contours cross each other. Scale invariance Property 1 implies that the critical points in span$[1, 1, \ldots, 1]$ are degenerate. $\square$

C.2.2. Bounds of $\mathcal{F}_{A,p,q}$ under constraints

For the MWB reduction to be valid, the contours are not allowed to cross each other nor cross the $V_k = 0$ plane. We enforce this restriction by a lower bound V_0 on the first contour V_1, and on the minimum inter-contour distance ϵ. We also want to build finite support distribution by imposing an upper parallel velocity bound V_M. We now rephrase the problem of finding the minimum (resp. maximum) of $\mathcal{F}_{A,p,q}$ as a constrained nonlinear minimization (resp. maximization) problem. Following standard notation in optimization theory, the $N+1$ inequality constraint functions are noted $g_i(V)$, the equality constraints $h_i(V)$ being nonexistent in our case.

Definition 2. Let us first give explicit forms for the constraint functions

$$\begin{aligned} g_1(V) &:= V_0 - V_1, && i = 1, \\ g_i(V) &:= V_{i-1} - V_i + \epsilon, && i = 2, \ldots, N, \\ g_{N+1}(V) &:= V_N - V_M, && i = N+1, \end{aligned} \tag{C.13}$$

We define the corresponding $N+1 \times N$ Jacobian matrix $(\nabla g)^T$ as the matrix whose ith row is $(\nabla g_i)^T$. Explicit form is straightforward from the definition of the g_i. For all j such that $1 \leqslant j \leqslant N$ we have

$$\begin{aligned} \tfrac{\partial g_1}{\partial V_j} &= -\delta_j^1, && i = 1, \\ \tfrac{\partial g_i}{\partial V_j} &= \delta_j^{i-1} - \delta_j^i, && i = 2, \ldots, N, \\ \tfrac{\partial g_{N+1}}{\partial V_j} &= \delta_j^N, && i = N+1. \end{aligned} \tag{C.14}$$

For clarity of notation, we note $\mathcal{F}_{A,p,q} = f$ with $q > p$ and $\mathcal{C} := (\mathbb{R}^{+*})^N$ in the following. The problem of finding the lower bound of f can be restated as

$$\begin{aligned} (P) \quad & \min_V f \\ \text{s.t.} \quad & g \leqslant 0 \\ & V \in \mathcal{C} \end{aligned} \tag{C.15}$$

The problem (P^*) for the upper bound can be defined similarly by minimizing $f^* = \mathcal{F}_{A,q,p} = 1/f, q > p$. We demonstrate results for P and precise when modifications (inequality inversions) are to be done for P^*. Let us recall the first-order necessary conditions of optimality (or Karush–Kuhn–Tucker (KKT) conditions) for the existence of a local minimum, without equality constraints.

Theorem 1. *Let $\overline{V}$ be a feasible point ($g(\overline{V}) \leqslant 0$) of P. If $\overline{V}$ is a local minimum then there exists $\lambda \in (\mathbb{R}^{+})^{N+1}$ such that*

$$\begin{aligned} & \nabla f + (\nabla g)^T \lambda = 0, \\ & \lambda_i \geqslant 0, \qquad i = 1, \ldots, N+1 \\ & \lambda_i g_i(\overline{V}) = 0, \qquad i = 1, \ldots, N+1. \end{aligned} \tag{C.16}$$

As the gradients of the constraints are constants, we can express the first of the above conditions in the simple form

$$(\nabla f)_j(\overline{V}) + \lambda_{j+1} - \lambda_j = 0, \; j = 1, \ldots, N. \tag{C.17}$$

We now establish a few properties of f for the feasible points of P.

Property 5. Let $\overline{V}$ be a feasible point of P. Then

$$(\nabla f)_1(\overline{V}) > 0, \tag{C.18}$$

$$(\nabla f)_N(\overline{V}) < 0. \tag{C.19}$$

Proof. Assume $\frac{\partial f}{\partial V_1} \leqslant 0$. Then from Property 3, for all $j > 1$ we have $\frac{\partial f}{\partial V_j} < 0$, and thus $\sum_j V_j \frac{\partial f}{\partial V_j} < 0$ which contradict the scale invariance property $\sum_j V_j \frac{\partial f}{\partial V_j} = 0$. The second inequality is proved similarly. □

Property 6. Let $\overline{V}$ be a feasible point of P^*. Then

$$(\nabla f)_1(\overline{V}) < 0, \tag{C.20}$$

$$(\nabla f)_N(\overline{V}) > 0. \tag{C.21}$$

Property 7. Let $\overline{V}$ be a feasible point of (P) (resp. (P^*)). If there exist j_1 such that $\nabla f_{j_1}(\overline{V}) = 0$, then it is unique.

Proof. Let us assume that there exists $j_2 \neq j_1$ such that $\frac{\partial f}{\partial V_{j_2}} = 0$. From Property 2 we deduce that $V_{j_1} = V_{j_2}$, which contradict the assumption that $\overline{V}$ is feasible, as at least one constraint is violated. □

From the two previous properties we deduce the sign of the gradient components.

Property 8. Let $\overline{V}$ be a feasible point of (P). There exists a unique j_1, such that exactly one of the following propositions is true.

- For all j such that $j < j_1, (\nabla f)_j > 0$ and for all $j \geqslant j_1, (\nabla_f)_j < 0$.
- For all j such that $j < j_1, (\nabla f)_j > 0, (\nabla_f)_{j_1} = 0$, and for all $j > j_1, (\nabla_f)_j < 0$.

Property 9. Let $\overline{V}$ be a feasible point of (P^*). There exists a unique j_1, such that exactly one of the following propositions is true.

- For all j such that $j < j_1, (\nabla_f)_j < 0$ and for all $j \geqslant j_1, (\nabla_f)_j > 0$.
- For all j such that $j < j_1, (\nabla_f)_j < 0, (\nabla_f)_{j_1} = 0$, and for all $j > j_1, (\nabla_f)_j > 0$.

Now we can deduce an ordering property for the KKT multipliers λ_i.

Property 10. Let $\overline{V}$ be a feasible point of (P) satisfying the KKT conditions (C.16). There exists a unique $j_1, 1 < j_1 < N+1$, such that exactly one of the two following statements is true.

- $\lambda_1 > \lambda_2 > \cdots > \lambda_{j_1} < \lambda_{j_1+1} < \cdots < \lambda_{N+1}$.
- $\lambda_1 > \lambda_2 > \cdots > \lambda_{j_1} = \lambda_{j_1+1} < \lambda_{j_1+2} < \cdots < \lambda_{N+1}$.

Proof. The ordering is a direct consequence of Property 8 and (C.17). □

Property 11. Let $\overline{V}$ be a feasible point of (P^*) satisfying the KKT conditions (C.16). There exists a unique $j_1, 1 < j_1 < N+1$, such that exactly one of the two following statements is true.

- $\lambda_1 < \lambda_2 < \cdots < \lambda_{j_1} > \lambda_{j_1+1} > \cdots > \lambda_{N+1}$.
- $\lambda_1 < \lambda_2 < \cdots < \lambda_{j_1} = \lambda_{j_1+1} > \lambda_{j_1+2} > \cdots > \lambda_{N+1}$.

We now restrict the set of possible extremal points by eliminating sets of points violating KKT conditions. Elimination is done first for the cases common to (P) and (P^*).

Property 12. Let $\overline{V}$ be a feasible point of (P) (resp. (P^*)). Let $I = \{i, g_i(\overline{V}) = 0\}$. If $\overline{V}$ satisfy the KKT conditions (C.16), then $\mathrm{card}(I) \in \{N, N-1\}$.

Proof. Let us first consider the trivial case $\mathrm{card}(I) = N+1$. In that case, all constraints are saturated. This can only happen if the choice of parameters V_0, V_M, ϵ is such that the system $g = 0$ has a solution, reducing the feasible set of solutions to that unique point. In that case $V_j = V_0 + (j-1)\epsilon$ for all j and $V_M = V_N = V_0 + (N-1)\epsilon$. In that case f is constant. We consider from now on that the parameters are chosen to forbid this case.

Now let us assume that $\mathrm{card}(I) < N-1$. Then there exist $i_1 < i_2 < i_3$ such that $\lambda_{i_1} = \lambda_{i_2} = \lambda_{i_3} = 0$. This is in contradiction with Property 10 (resp. Property 11). □

If the parameters are set to exclude the special case $card(I) = N+1$, the local minimum can thus only be found on a vertex ($card(I) = N$) or an edge ($card(I) = N-1$) of the constraints polytope.

Definition 3. Let $1 \leqslant i \leqslant N+1$. The vertex $V^{(i)}$ is the unique solution of the system $g_k(V^i) = 0, k \neq i$. The components of $V^{(i)}$ are of the form

$$\begin{aligned} V_j^{(i)} &= V_0 + (j-1)\epsilon, \quad 1 \leqslant j \leqslant i-1, \\ V_j^{(i)} &= V_M - (N-j)\epsilon, \quad i \leqslant j \leqslant N. \end{aligned} \tag{C.22}$$

Definition 4. Let $1 \leqslant i < N+1$. The edge $E^{(i,i+1)}$ is the set of points V solution of

$$\begin{aligned} g_k(V) &= 0, \quad k \neq i, i+1 \\ g_k(V) &< 0, \quad k = i, i+1. \end{aligned} \tag{C.23}$$

The components of a point V of $E^{(i,i+1)}$ satisfy the following relations

$$\begin{aligned} V_j^{(i,i+1)} &= V_0 + (j-1)\epsilon, && 1 \leqslant j \leqslant i-1, \\ V_j^{(i,i+1)} &= V_M - (N-j)\epsilon, && i+1 \leqslant j \leqslant N, \\ V_0 + (i-1)\epsilon &< V_i^{(i,i+1)} < V_M - (N-i)\epsilon, && j = i. \end{aligned} \tag{C.24}$$

We have here implicitly discarded all the edges of the general form $E^{(i_1,i_2)}$ which would obviously contradict Property 10 (resp. 11). Vertex $V^{(i)}$ corresponds to the situation where the first $i-1$ contours are closest to V_0 and the $N-i+1$ remaining contours are closest to V_M. In the case of an edge $E^{(i,i+1)}$, the first $i-1$ contours are closest to V_0, the last $N-i$ contours are closest to V_M and V_i is free to move between $V_{i-1} + \epsilon$ and $V_{i+1} - \epsilon$. A representation of the contours values for the vertices and edges is given in Fig. C.21.

Property 13 (*Restriction on admissible solution vertices).* Let $V^{(i)}$ be a vertex, as defined in Definition 3. If $V^{(i)}$ is a solution of (P) then

$$2 \leqslant i \leqslant N. \tag{C.25}$$

Proof. Let us assume that $i = 1$. From (C.17) we then have $(\nabla f)_1 = -\lambda_2$. From Property 5 we deduce that $\lambda_2 < 0$ which contradicts the KKT conditions $\lambda_j > 0, j \neq i$. The case $i = N+1$ is excluded similarly. □

The previous restriction does not apply to (P^*) as the gradient component signs are compatible with Property 6.

Property 14 (*Admissible solutions of* (P) *(resp.* (P^*)*) on an edge).* Let $E^{(i,i+1)}$ an edge as defined in Definition 4. If $\overline{V} \in E^{(i,i+1)}$ is a local minimum of f (resp. f^*) then

$$2 \leqslant i \leqslant N-1. \tag{C.26}$$

Proof. Let us assume that $i = 1$. We then have $\lambda_1 = \lambda_2 = 0$. From (C.17) we deduce that $(\nabla f)_1 = 0$, which contradicts Property 5 (resp. 6). The case $i = N$ is excluded similarly. □

Considering now both (P) and (P^*) we have so far proved that the extremal values of f can be reached on some of the $N+1$ vertices $V^{(i)}$, or on critical points on some of the N edges $E^{i,i+1}$. Further restrictions are not possible without additional assumptions on the values of the parameters V_0, V_M, ϵ and the weights A_j. We now give explicit expressions for the values of f for those possible extremal points.

Property 15 (*Values of* f *on the vertices).* Let $1 \leqslant i \leqslant N+1$. We have

$$f(V^{(i)}) = \frac{\left(q+\frac{1}{2}\right)^{2p+1}}{\left(p+\frac{1}{2}\right)^{2q+1}} \frac{\left(\Sigma^0_{p,i-1} + \Sigma^M_{p,i}\right)^{2q+1}}{\left(\Sigma^0_{q,i-1} + \Sigma^M_{q,i}\right)^{2p+1}}, \tag{C.27}$$

with

$$\begin{aligned} \Sigma^0_{l,k} &:= \sum_{j=1}^{k} A_j (V_0 + (j-1)\epsilon)^{2l+1}, \\ \Sigma^M_{l,k} &:= \sum_{j=k}^{N} A_j (V_M - (N-j)\epsilon)^{2l+1}. \end{aligned} \tag{C.28}$$

Property 16 (*Values of* f *on critical points of the edges).* Let $1 \leqslant i \leqslant N$. If a local extremum $V^{(i,i+1)}$ of f exists on the edge $E^{(i,i+1)}$ then

$$V_i^{(i,i+1)} = \left(\frac{\Sigma^0_{q,i-1} + \Sigma^M_{p,i+1}}{\Sigma^0_{p,i-1} + \Sigma^M_{p,i}} \right)^{\frac{1}{2(q-p)}} \tag{C.29}$$

with the existence condition

$$V_0 + (i-1)\epsilon < V_i^{(i,i+1)} < V_M - (N-i)\epsilon. \tag{C.30}$$

We then have

$$f(V^{(i,i+1)}) = \frac{\left(q+\frac{1}{2}\right)^{2p+1}}{\left(p+\frac{1}{2}\right)^{2q+1}} \frac{\left(\Sigma^0_{p,i-1} + \Sigma^M_{p,i+1} + A_i (V_i^{(i,i+1)})^{2p+1}\right)^{2q+1}}{\left(\Sigma^0_{q,i-1} + \Sigma^M_{q,i+1} + A_i (V_i^{(i,i+1)})^{2q+1}\right)^{2p+1}}. \tag{C.31}$$

We thus define the binding constants by

$$m_{A,p,q,\epsilon,V_0,V_M} = \min_i \left\{ f(V^{(i)}), f(V^{(i,i+1)}) \right\}, \tag{C.32}$$

and

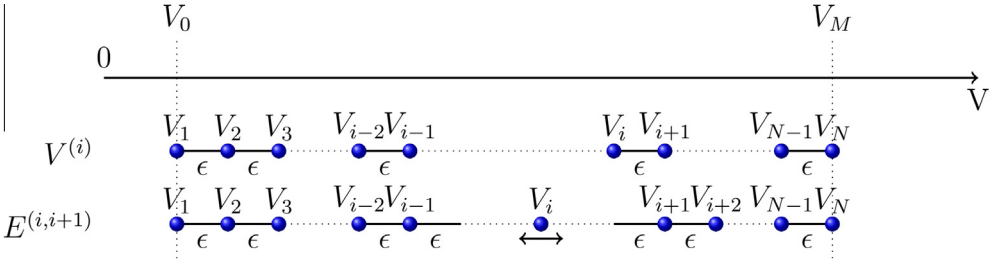

Fig. C.21. Positions of the contours for a vertex $V^{(i)}$ and an edge $E^{(i,i+1)}$ of the constraints polytope.

$$M_{A,p,q,\epsilon,V_0,V_M} = \max_i \left\{ f(V^{(i)}),\ f(V^{(i,i+1)}) \right\}, \tag{C.33}$$

where only admissible values are selected.

C.3. Prefactor bounds in the Maxwellian case

Let us consider the case where a MWB distribution, whose contours obey the constraints g_i, verify exact moment equivalence with a Maxwellian distribution for the N first even order moments. For $0 \leqslant p, q \leqslant N-1$ we have

$$m_{A,p,q,\epsilon,V_0,V_M} < \frac{\left(\mathcal{M}^C_{2p}\right)^{2q+1}}{\left(\mathcal{M}^C_{2q}\right)^{2p+1}} < M_{A,p,q,\epsilon,V_0,V_M}. \tag{C.34}$$

At order $2p$ the Maxwellian moment reads

$$\mathcal{M}^C_{2p} = nT^p J_{2p}, \tag{C.35}$$

where $J_{2p} = \frac{(2p)!}{2^p (p)!}$. Setting the Maxwellian prefactor $\alpha = \frac{n}{\sqrt{T}}$ we have

$$m_{A,p,q,\epsilon,V_0,V_M} < \alpha^{2(q-p)} \frac{J_{2p}^{2q+1}}{J_{2q}^{2p+1}} < M_{A,p,q,\epsilon,V_0,V_M}, \tag{C.36}$$

And thus α bounds for $q > p$

$$\left(m_{A,p,q,\epsilon,V_0,V_M} \frac{J_{2q}^{2p+1}}{J_{2p}^{2q+1}} \right)^{\frac{1}{2(q-p)}} < \alpha < \left(M_{A,p,q,\epsilon,V_0,V_M} \frac{J_{2q}^{2p+1}}{J_{2p}^{2q+1}} \right)^{\frac{1}{2(q-p)}}. \tag{C.37}$$

Note that these bounds do not provide a close estimate of the actual extensibility of the distribution, as they are reached when most or all of the constraints are saturated. The actual α range achievable from a starting vector V has a strong nonlinear dependency on V which prevents defining closer a priori bounds.

References

[1] N. Besse, P. Bertrand, Gyro-water-bag approach in nonlinear gyrokinetic turbulence, J. Comput. Phys. (228) (2009) 3973–3995.
[2] A. Brizard, T. Hahm, Foundations of nonlinear gyrokinetic theory, Rev. Mod. Phys. 79 (2007) 421–468.
[3] V. Grandgirard, M. Brunetti, P. Bertrand, N. Besse, X. Garbet, P. Ghendrih, G. Manfredi, Y. Sarazin, O. Sauter, E. Sonnendrçker, J. Vaclavik, L. Villard, A drift-kinetic semi-lagrangian 4d code for ion turbulence simulation, J. Comput. Phys. 217 (2) (2006) 395–423.
[4] V. Grandgirard, Y. Sarazin, P. Angelino, A. Bottino, N. Crouseilles, G. Darmet, G. Dif-Pradalier, X. Garbet, P. Ghendrih, S. Jolliet, G. Latu, E. Sonnendrücker, L. Villard, Global full-f gyrokinetic simulations of plasma turbulence, Plasma Phys. Contr. F 49 (12B) (2007) B173.
[5] V. Grandgirard, Y. Sarazin, X. Garbet, G. Dif-Pradalier, P. Ghendrih, N. Crouseilles, G. Latu, E. Sonnendrçker, N. Besse, P. Bertrand, Computing ITG turbulence with a full-f semi-lagrangian code, Commun. Nonlinear Sci. 13 (1) (2008) 81–87.
[6] S. Jolliet, A. Bottino, P. Angelino, R. Hatzky, T. Tran, B. Mcmillan, O. Sauter, K. Appert, Y. Idomura, L. Villard, A global collisionless pic code in magnetic coordinates, Comput. Phys. Commun. 177 (5) (2007) 409–425.
[7] T. Görler, X. Lapillonne, S. Brunner, T. Dannert, F. Jenko, F. Merz, D. Told, The global version of the gyrokinetic turbulence code gene, J. Comput. Phys. 230 (18) (2011) 7053–7071.
[8] X. Garbet, Y. Idomura, L. Villard, T. Watanabe, Gyrokinetic simulations of turbulent transport, Nucl. Fusion 50 (4) (2010) 043002.
[9] N. Besse, On the Cauchy problem for the gyro-water-bag model, Math. Mod. Math. Appl. Sci. (21) (2011) 1839–1869.
[10] P. Morel, E. Gravier, N. Besse, R. Klein, A. Ghizzo, P. Bertrand, X. Garbet, P. Ghendrih, V. Grandgirard, Y. Sarazin, Gyrokinetic modelling: a multi water bag approach, Phys. Plasmas 14 (11) (2007) 112109.
[11] P. Morel, E. Gravier, N. Besse, A. Ghizzo, P. Bertrand, The water bag model and gyrokinetic applications, Commun. Nonlinear Sci. 13 (2008) 11–17.
[12] B.D. Fried, S. Conte, The Plasma Dispersion Function, Academic Press, New York NY, 1961.
[13] D.K. Salkuyeh, A note on a three-term recurrence for a tridiagonal matrix, Appl. Math. Comput. 176 (2) (2006) 442–444.
[14] M. El-Mikkawy, Comments on a note on a three-term recurrence for a tridiagonal matrix, Appl. Math. Comput. 139 (2–3) (2003) 503–511.
[15] B. Davies, Locating the zeros of an analytic function, J. Comput. Phys. 66 (1) (1986) 36–49.
[16] P. Kravanja, M. van Barel, Computing the Zeroes of Analytic Functions, Springer, Berlin, 2000.
[17] A.C. Calder, J.G. Laframboise, Multiple-water-bag simulation of inhomogeneous plasma motion near an electrode, J. Comput. Phys. 65 (1) (1986) 18–45.
[18] M. Brunetti, V. Grandgirard, O. Sauter, J. Vaclavik, L. Villard, A semi-lagrangian code for nonlinear global simulations of electrostatic drift-kinetic ITG modes, Comput. Phys. Commun. (163) (2004) 1–21.